Generative Data Assimilation for Surface Ocean State Estimation from Multi-Modal Satellite Observations

Scott A. Martin[1], Georgy E. Manucharyan[1], and Patrice Klein[2,3,4]

[1]School of Oceanography, University of Washington, Seattle, WA, USA
[2]Environmental Science and Engineering, California Institute of Technology, Pasadena, CA, USA
[3]Jet Propulsion Laboratory, California Institute of Technology, Pasadena, CA, USA
[4]LMD-IPSL, ENS, PSL Université, Ecole Polytechnique, Sorbonne Université, CNRS, Paris, France

Key Points:

- We develop a generative data assimilation method to estimate sea surface height, temperature, salinity, and currents from satellites.
- By training a diffusion model on high-resolution ocean model simulations, we ensure state estimation with realistic dynamics across scales.
- Our method skillfully predicts surface currents and frontal scale salinity in an unsupervised manner, using only satellite observables.

Corresponding author: Scott A. Martin, `smart1n@uw.edu`

Abstract

Estimating the surface ocean state at mesoscale eddy-resolving scales is essential for understanding the role of eddies in climate and marine ecosystems. Satellites provide multi-modal observations through sea surface height, temperature (SST), and salinity (SSS). However, each variable is observed with varying resolutions and sparsity, while some variables, such as surface currents, are not yet observed by satellites. All these variables must be accurately reconstructed across scales to study eddy dynamics. Dynamical data assimilation (DA) struggles to accurately reconstruct eddies since, to respect the equations of motion, it must reconstruct both the surface and interior ocean state, but the interior is sparsely observed. Relaxing this requirement and focusing only on the surface could improve surface state estimation, but a new method is required to ensure reconstructions remain physically realistic. Here, we introduce a score-based generative data assimilation (GenDA) framework for jointly reconstructing key surface ocean variables at eddy-resolving scales from multi-modal satellite observations. GenDA uses a two-stage approach: training a score-based diffusion model on a simulation to generate realistic ocean states before employing this as a Bayesian prior to assimilate sparse observations and generate state estimates. The learned diffusion prior leads to coherence between variables and realism across scales. By synergizing low-resolution SSS with high-resolution SST observations, GenDA improves the SSS resolution. Remarkably, GenDA can infer unobserved surface currents using only satellite observables, suggesting the learned prior encodes physical relationships between variables. Applied to real observations, GenDA demonstrates strong generalizability compared to regression-based deep learning and outperforms state-of-the-art dynamical DA.

Plain Language Summary

Oceans play a key role in climate and marine ecosystems, with swirling currents called eddies shaping the transport of heat and nutrients. Satellites help track the ocean's surface by measuring temperature, salinity, and sea level, but each measurement has large gaps or low resolution. Surface currents, which are crucial for understanding ocean dynamics, are not yet directly observed by satellites. Traditional methods that combine observations with physics-based models struggle to reconstruct these small-scale features because they must also estimate the deeper ocean, which is sparsely observed. We propose a new approach, called Generative Data Assimilation (GenDA), which uses diffusion models – a type of artificial intelligence (AI) model used widely for image generation - to improve surface ocean state estimates. First, a diffusion model is trained on simulated ocean data to learn realistic patterns. Then, this knowledge helps combine sparse satellite observations into high-resolution reconstructions of the ocean's surface. GenDA enhances low-resolution salinity observations and even infers unobserved surface currents, suggesting it has learned key physical relationships from the simulation. When tested on real-world observations, GenDA outperforms both traditional physics-based methods and other AI techniques. This approach could lead to better high-resolution surface ocean monitoring from space.

1 Introduction

1.1 Background & Motivation

1.1.1 Conventional Methods for Surface Ocean State Estimation

Estimating the dynamical state of the surface ocean at sufficiently high resolution to resolve mesoscale eddies and their associated fronts and filaments ('eddy-resolving' hereafter) is fundamental for research into air-sea fluxes (Rai et al., 2021; Seo et al., 2023), vertical ocean heat transfer (Siegelman et al., 2020), and the influence of eddies on marine ecosystems (Lévy et al., 2018; Zhang et al., 2019). A large volume of surface ocean observations come from satellites that observe sea surface height (SSH), sea surface temperature (SST), and sea surface salinity (SSS). Each variable is observed at varying resolutions and with often large spatial and/or temporal gaps between satellite passes or due to cloud occlusion (Figure 1). In the case of SSH, the sampling is particularly sparse, with only point-wise measurements along satellite tracks typically separated by tens to hundreds of kilometers in space and days to weeks in time. The recent launch of the first wide-swath satellite altimeter, SWOT (Fu et al., 2024), now provides groundbreaking 2D snapshots of SSH, but its 21-day orbital return time still leaves large spatiotemporal gaps (Archer et al., 2025). Other dynamical variables, such as surface currents remain entirely unobserved by satellites and must thus be inferred either from sparse in situ observations or indirectly from SSH. The proposed ODYSEA mission could in future help to address this crucial gap in the satellite observing system (Torres et al., 2023). Estimating the dynamical state of the surface ocean, defined here as the 2D SSH, SST, SSS, and surface current velocity fields from sparse multi-modal satellite observations (SSH, SST, & SSS) is hereafter referred to as 'surface ocean state estimation'. While recent studies have developed approaches to reconstruct single variables at eddy-resolving scales (e.g. Martin et al. (2024b)), eddy-resolving surface ocean state estimation requires jointly reconstructing SSH, SST, SSS, and surface currents while maintaining dynamical consistency between variables across scales. This is beyond the current capabilities of both dynamical and novel data-driven approaches and in this study we seek to address this.

One approach to state estimation is to assimilate observations, both satellite and in situ, into an ocean general circulation model (GCM) using data assimilation. By leveraging a GCM in the state estimation process, data assimilation ensures the reconstructed state satisfies the equations of motion for ocean dynamics while minimizing the misfit to observations. In order to satisfy the equations of motion, GCM data assimilation must reconstruct the full 3D ocean state rather than just surface fields. This requires in situ observations to constrain the ocean interior, but in situ observations are significantly more sparse than satellite observations of the surface, leading to suboptimal surface state estimation. The highest-resolution global data assimilation products (e.g. GLORYS 12 (Lellouche et al., 2021)) do not yet accurately resolve mesoscale eddies, showing high errors when compared to satellite observations of SSH or SST compared to statistical approaches like objective analysis (Lellouche et al., 2021). Additionally, performing data assimilation with ocean GCMs of sufficiently high resolution to fully resolve ocean eddy dynamics is computationally prohibitive. For instance, the 1/12° GCM used in GLORYS 12 is too coarse to resolve submesoscale dynamical processes that can affect the formation and evolution of mesoscale eddies (Taylor & Thompson, 2023). These challenges are circumvented by data assimilation schemes for idealized, single-layer models of surface ocean dynamics (Le Guillou et al., 2021, 2023, 2024); however, such idealized models by design make stringent assumptions about ocean dynamics that do not hold in general in the real world.

Due to the limitations of dynamical data assimilation, most state-of-the-art gridded satellite products are generated using statistical objective analysis methods, such as optimal interpolation (OI) (Bretherton et al., 1976). In OI, linear least squares estimation predicts the missing SSH, SST, or SSS values in the gaps between observations based on a covariance model specified a priori. OI is a statistical method with no mechanism to ensure the equations of motion are respected in the resulting state estimate, in contrast to DA. By relaxing the requirement to satisfy dynamical equations, and by focusing only on surface fields, OI achieves significantly smaller errors compared to independent observations than DA. However, OI typically results in overly smooth and physically unrealistic reconstructed fields, with inaccurate representations of mesoscale eddies (Ballarotta et al., 2019). Additionally, OI produces incoherent estimates across different observables, with different effective resolutions for each observable, which are typically each mapped separately. OI also cannot provide a mechanism for estimating variables that were never observed, like surface currents. Consequently, surface currents are

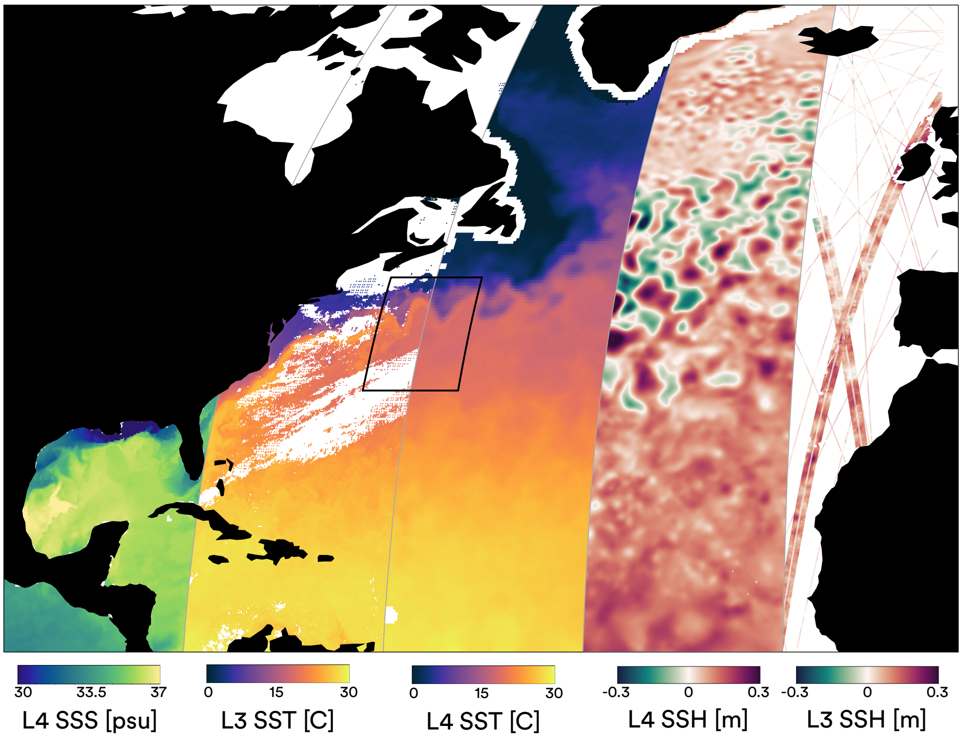

Figure 1. Illustration of the available multi-modal satellite observations of the surface ocean state. Satellite observations are available at both 'Level 3' (L3) and 'Level 4' (L4) processing levels. L3 observations are before any interpolation, so are sparse but high-resolution, whereas L4 has been interpolated to a gap-free grid, smoothing smaller scales (e.g. using objective analysis). From left to right: L4 SSS from E.U. Copernicus Marine Service Information (CMEMS) (2024e), L3 SST from E.U. Copernicus Marine Service Information (CMEMS) (2024a), L4 SST from Remote Sensing Systems (2017), L4 SSH from Martin et al. (2024a), and L3 SSH from both nadir (E.U. Copernicus Marine Service Information (CMEMS), 2024b) and SWOT (AVISO/DUACS, 2024) altimeters. Observations shown here are for 2024-04-05. The boxed region is the study region considered in our experiments.

usually derived from the OI-mapped SSH field under the assumption of geostrophy which holds only at mesoscale and larger (Le Traon et al., 1998; Taburet et al., 2019).

1.1.2 Deep Learning Approaches: Observation Vs. Simulation Learning

In recent years, data-driven deep learning methods have been increasingly adopted in satellite oceanography to better resolve ocean eddies. Deep learning approaches seek to solve satellite oceanography inverse problems using deep neural networks trained on large quantities of either real or simulated ocean data. Applications considered by past studies include: high-resolution SSH mapping from satellite altimetry and SST (Fablet et al., 2021; Manucharyan et al., 2021; Buongiorno Nardelli et al., 2022; Beauchamp et al., 2022; Martin et al., 2023; Archambault et al., 2023; Fablet et al., 2023, 2024; Ciani et al., 2024; Febvre et al., 2024; Archambault, Filoche, Charantonis, Béréziat, & Thiria, 2024; Archambault, Filoche, Charantonis, & Béréziat, 2024; Martin et al., 2024b), filling in the gaps in high-resolution infrared SST observations caused by clouds (Agabin et al., 2024; Goh et al., 2023; Fanelli et al., 2024), and inferring ageostrophic surface currents from SSH/SST (Sinha & Abernathey, 2021; Fablet et al., 2023; Xiao et al., 2023; Fablet et al., 2024). A number of studies have demonstrated that deep learning provides an effective way to synergize multiple satellite observables to improve performance (Sinha & Abernathey, 2021; Buongiorno Nardelli et al., 2022; Martin et al., 2023; Fablet et al., 2023; Archambault et al., 2023; Fablet et al., 2024; Ciani et al., 2024; Martin et al., 2024b; Archambault, Filoche, Charantonis, Béréziat, & Thiria, 2024; Archambault, Filoche, Charantonis, & Béréziat, 2024; Kugusheva et al., 2024). While there are differences between these past studies in terms of objective, training data, and neural network architecture, they typically share the same overarching framework: supervised learning is used to train a neural network to solve a certain class of satellite oceanography inverse problem for a given observing system.

For certain satellite oceanography problems, neural networks can be trained directly on real-world observations without using synthetic data from GCM simulations in any way. For SSH mapping from nadir altimeters, it has been shown that the large volume of past real-world satellite SSH and SST observations is sufficient to train a neural network to map SSH at eddy-resolving scales (Martin et al., 2023; Archambault et al., 2023; Martin et al., 2024b; Archambault, Filoche, Charantonis, Béréziat, & Thiria, 2024), recently achieving state-of-the-art global SSH mapping (Martin et al., 2024b). However, these observation-only learning methods are only applicable to tasks for which there are sufficiently dense real-world observations of the target variable to construct a training dataset. This is unlikely to be the case for many surface ocean variables, for example ageostrophic surface currents which are only sparsely observed by drifters, or SSS which is only observed at relatively low resolution from satellites. Additionally, the sparsity and sensor noise in real-world observations mean observation-only learning typically results in reconstructions that are overly smooth compared to numerical simulations (e.g. Archambault, Filoche, Charantonis, Béréziat, and Thiria (2024)).

To address the limitations of observation-only learning, a number of studies have proposed 'simulation learning' approaches where synthetic data from ocean GCMs is used during training. In these approaches, a neural network is typically trained in a supervised regression setting, using pseudo-observations sampled from a GCM as inputs and the corresponding complete GCM target fields as ground truth labels (Beauchamp et al., 2022; Fablet et al., 2023; Febvre et al., 2024; Fablet et al., 2024; Agabin et al., 2024; Goh et al., 2023; Archambault, Filoche, Charantonis, Béréziat, & Thiria, 2024; Archambault, Filoche, Charantonis, & Béréziat, 2024). During inference, the trained network receives real-world observations and generates a state estimate that mirrors the characteristics of the GCM it was trained on (Febvre et al., 2024). Analogous to data assimilation, simulation learning seeks to generate a state estimate with dynamics resembling that of a GCM. However, there is no explicit mechanism to ensure the equations of motion are respected, so simulation learning does not ensure dynamical consistency in as strict a sense as dynamical data assimilation.

While simulation learning approaches are a promising avenue for surface ocean state estimation, the supervised regression framework described above has a number of limitations:

1. Even subtle discrepancies between the pseudo-observations and real-world observations may propagate unpredictably through the network at inference. This often requires fine-tuning on real-world data (Archambault, Filoche, Charantonis, & Béréziat, 2024), which is challenging for sparsely-observed variables like ageostrophic surface currents.
2. Supervised regression seeks to predict a single state estimate that has the smallest average error (e.g. mean square error (MSE)). This induces a spectral bias where

the large-scale signals dominate the MSE, leading to overly-smooth predictions with artificially steep spectral slopes.

3. Supervised regression typically provides no natural metric of uncertainty for the resulting state estimate.
4. Supervised regression requires bespoke training for each observing system, necessitating computationally expensive re-training each time the input observing system or the GCM pseudo-observation sampling strategy is altered.

Ideally, a deep learning method for surface ocean state estimation would address the above points. In addition, it would be desirable to obtain multi-variate surface state estimates where multiple variables are reconstructed jointly, preserving the dynamical consistency between variables across scales. This coherence between variables across scales is crucial for evaluating dynamical diagnostics such as eddy fluxes and frontogenesis rates.

1.1.3 A Generative Deep Learning Approach to Simulation Learning

Traditional data assimilation uses methods like Kalman filters or variational methods that work well for linear systems but they struggle with highly nonlinear systems, high-dimensional data, and uncertainty in measurements. Diffusion models (Song & Ermon, 2019; Karras et al., 2022; Croitoru et al., 2023) are generative deep learning models that can naturally learn complex probability distributions of data, making them ideal for highly nonlinear systems, such as oceanic and atmospheric turbulence. Manshausen et al. (2024) recently highlighted the strong potential of generative data assimilation based on these diffusion models for reconstructing atmospheric weather from sparse observations.

To address the shortcomings of simulation learning approaches, in this study we explore the efficacy of generative diffusion models for surface ocean state estimation. Unlike in the regression formulation, generative models seek to model the full distribution of the training data, mapping from random latent vectors to 'realistic' examples from the desired distribution - see Buzzicotti (2023) for a review of generative models and their application to data reconstruction in complex flows. Diffusion models generate realistic examples by learning to reverse a prescribed forward process that degrades the data, typically through the addition of Gaussian noise. Applying the trained diffusion model to random noise fields then allows to generate realistic, but random, samples from the data distribution (Song & Ermon, 2019; Karras et al., 2022; Croitoru et al., 2023) (Section 2.1.1). For surface ocean state estimation, generative models could allow to retain fine-scale features and dynamical consistency between variables in the output by producing state estimates that 'look like' examples from the training distribution - in our case, multi-variate snapshots from high-resolution GCM simulations. The primary challenge in using generative models for state estimation is controlling the output such that the 'realistic' samples generated correspond well to available observations. One approach is to use conditional diffusion models, where a model is trained to generate high-resolution examples conditioned on both random noise and a low-resolution degradation of the data (S. Wang et al., 2024; Han et al., 2024; Ghosh et al., 2024). However, this approach, like the supervised regression approach, requires careful design of training pairs such that the low-resolution data degradations are representative of the inputs available in the real world at inference. Instead, we here explore an approach that requires no generation of pseudo-observations from a GCM.

Score-based data assimilation (also referred to here as 'generative data assimilation') overcomes the challenge of controlled generation in a way that decouples the neural network training from the observing system using a two-stage strategy (Rozet & Louppe, 2023a). First, an unconditional, score-based diffusion model is trained to generate realistic samples from a high-resolution training dataset (e.g. GCM output). Second, the generation procedure of the diffusion model is guided in a Bayesian manner using observations (with no re-training of the diffusion model) such that the output fits sparse or degraded observations while preserving the learned characteristics of the training data (Rozet & Louppe, 2023a, 2023b) (Section 2.1.2). Since the diffusion model is trained only on full model fields, the learned network weights are not specific to the observing system used at inference. Properties of the observing system are all encoded in the observation operator used to guide the generation at inference (Section 2.1.3). This allows training a single diffusion model then using it for inference with a wide range of observing systems with no additional re-training. Even when certain variables, like surface currents, are unobserved, the diffusion model still predicts them in a way that should remain dynamically consistent through the learned relationships to the observed variables.

Generative data assimilation was recently shown to be effective for producing 3km-resolution atmospheric state estimates from sparse weather station observations (Manshausen et al., 2024). Notably, Manshausen et al. (2024) demonstrated this method had promising 'channel synthesis' capabilities that allowed estimating a completely unobserved variable (meridional winds) from observations of other atmospheric state variables with reasonable accuracy and qualitative physical realism. Channel synthesis is crucial in surface ocean state estimation since many quantities of interest (e.g. ageostrophic surface currents) are only sparsely observed by in situ platforms but have strong signatures on satellite observables like SSH, SST, and SSS (Sinha & Abernathey, 2021; Fablet et al., 2023, 2024).

1.2 Our Contributions

Here, we adapt and apply the generative data assimilation method (referred to as 'GenDA' hereafter) developed for atmospheric reanalysis in Manshausen et al. (2024) to the closely-related problem of eddy-resolving surface ocean state estimation. We demonstrate that GenDA, trained on a GCM-based data assimilation product (GLORYS 12), is capable of solving realistic satellite oceanography inverse problems without bespoke training for each observing system.

Using an observing system simulation experiment, we compare GenDA to a baseline supervised learning approach trained for one specific observing system. We build upon the observation operator used in Manshausen et al. (2024) by adding coarse-graining terms to allow incorporating information from existing low-resolution satellite SSH, SST, and SSS products (e.g. those created using OI), ensuring the accuracy at large scales of the GenDA state estimates. The method proposed here is the first deep learning approach, to our knowledge, that allows to jointly reconstruct the full surface ocean state vector (SSH, SST, SSS, and surface currents).

Finally, we explore the ability of GenDA to generalize to real-world observations through an observing system experiment. We demonstrate that GenDA generalizes from simulation training to real-world inference better than a baseline supervised learning approach, with lower errors and improved physical realism. The resulting GenDA real-world surface ocean state estimates preserve the dynamical characteristics of the simulation data used during training. GenDA's generative formulation reduces the spectral bias in regression-based approaches, exhibiting realistic dynamics across scales. GenDA has significantly smaller errors against independent satellite observations than a state-of-the-art dynamical data assimilation system.

2 Methods

2.1 GenDA: Generative Data Assimilation

We seek to estimate the 2D dynamical state of the surface ocean which we represent using a state vector, x. Concretely, x here will be (SSH, SST, SSS, u_{ageo}, v_{ageo}) at

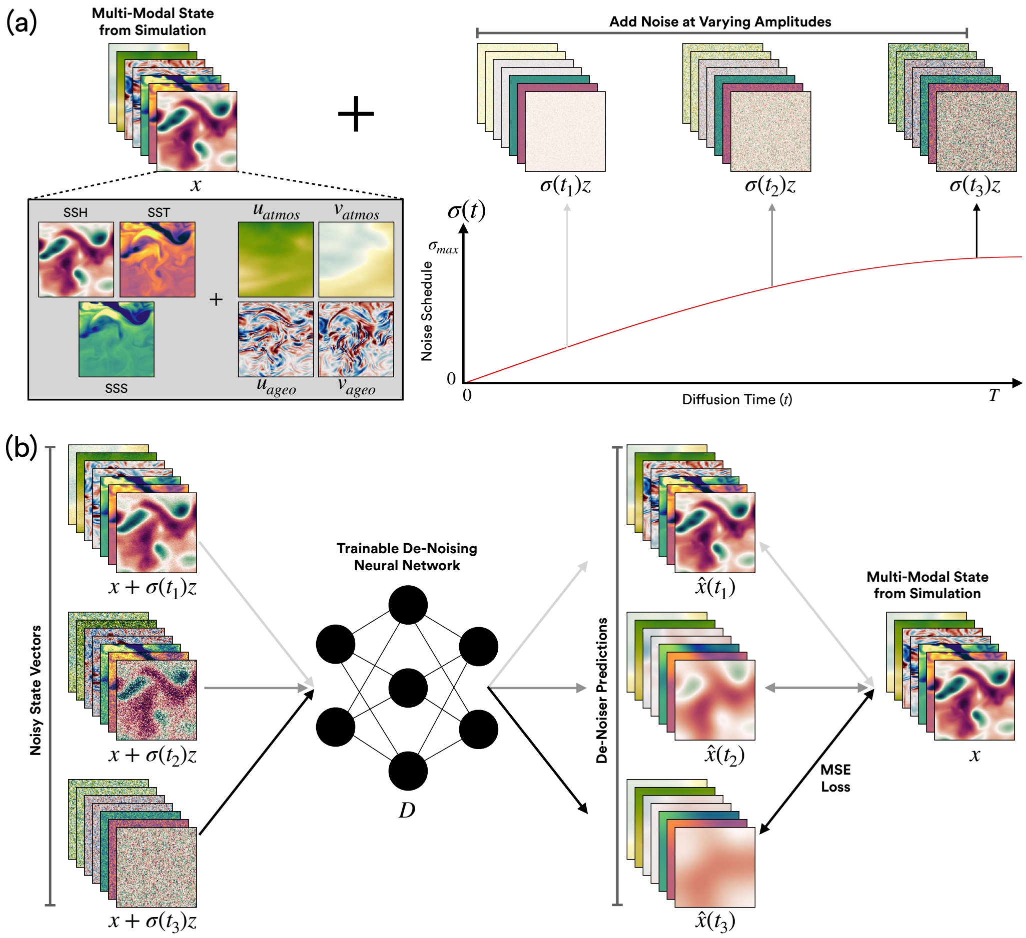

Figure 2. Schematic of the GenDA training phase. (a) Gap-free, multi-modal state vectors, x, are taken from the simulation training data and Gaussian white noise, $\sigma(t)z$, at varying amplitudes is added. (b) A de-noising neural network, D, is trained to map from noisy states, $x+\sigma(t)z$ to de-noised states, $\hat{x}(t)$, by minimizing MSE between $\hat{x}(t)$ and x.

each point on a regular 2D grid, where u_{ageo} and v_{ageo} are the ageostrophic components of the zonal and meridional surface current velocities respectively. Note, we reconstruct only the ageostrophic surface currents to focus GenDA on reconstructing currents not directly retrievable from SSH. We define the ageostrophic surface current to be the residual between the total surface current and that predicted from SSH assuming geostrophic balance. To estimate x, we use potentially sparse or degraded (e.g coarse-grained or noisy) observations, y, which are the result of applying an observation operator, $\mathcal{A}$, to the state vector,

$$y = \mathcal{A}(x). \tag{1}$$

2.1.1 Score-Based Diffusion Models

Diffusion models are a powerful class of generative deep learning models, trained to generate realistic examples drawn from a distribution of training data like natural images or, in our case, snapshots from ocean GCM simulations. During training, a neural network, D, is trained to 'de-noise' examples from the training dataset by predicting the noise-free example from its noisy counterpart (Karras et al., 2022). In our case, D gives a prediction, $\hat{x}(t)$, of the noise-free ocean state vector, $x(t = 0)$, given its noisy counterpart, $x+\sigma(t)z$, where $\sigma(t)$ is a variable noise amplitude, z is a unit variance Gaussian noise vector with the dimensions of x, and t is a 'time' axis along which the amplitude of the noise added varies from 0 at $t = 0$ to σ_{max} at $t = T$ (Figure 2a). D is trained by minimizing MSE between $\hat{x}(t)$ and $x(t = 0)$ (Figure 2b).

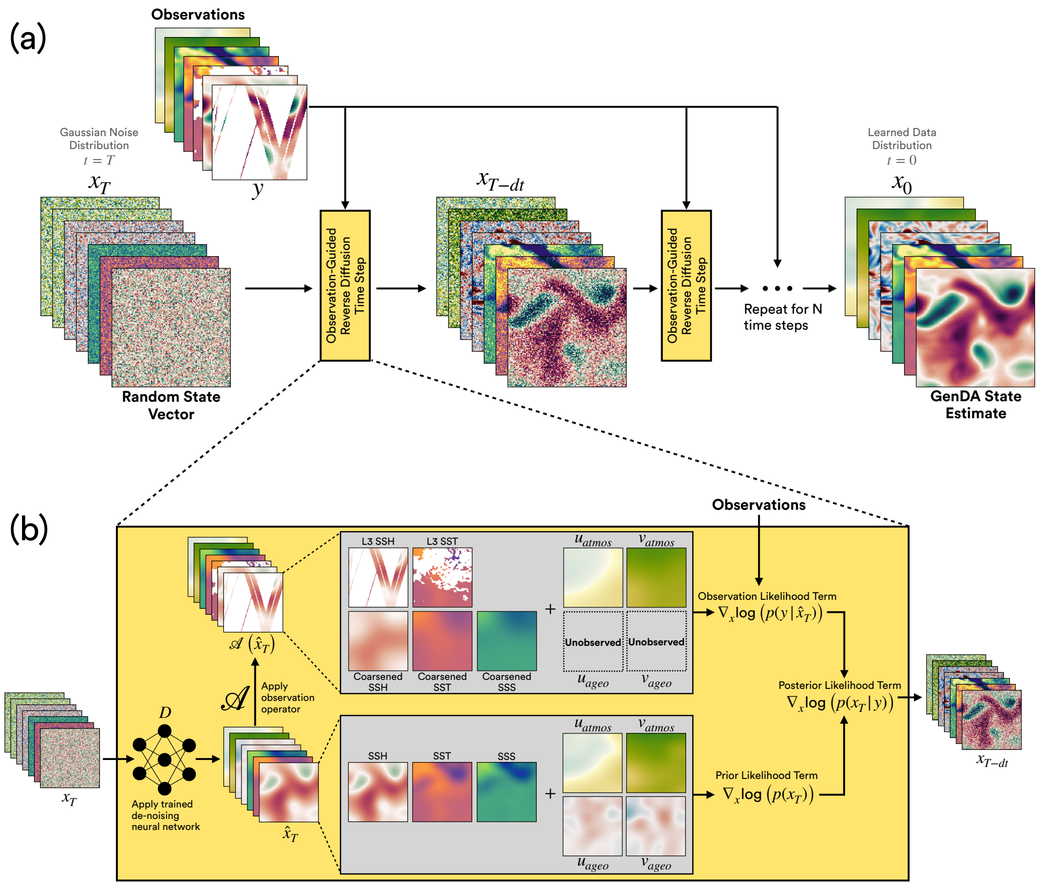

Figure 3. Schematic of the GenDA inference phase. (a) A random state, x_T, is mapped to a state estimate, x_0, through repeated observation-guided reverse time steps, reversing a forward noise process (Section 2.1), along the diffusion 'time' axis from $t = T$ (noise distribution) to $t = 0$ (learned data distribution). An ensemble of state estimates is generated by inputting different random states, x_T. (b) Within each reverse time step, the trained de-noising neural network, D, is applied, predicting a de-noised state, $\hat{x}_t$, which is compared to observations, y, through the observation operator, $\mathcal{A}$. Combining the prior likelihood gradient from D, $\nabla_x (p(x_t))$, with the observation likelihood term, $\nabla_x (p(y|\hat{x}_t))$, a reverse time step is made using $\nabla_x (p(x_t|y))$ to maximize the posterior likelihood. The weights of D are kept fixed throughout this process.

Given a trained de-noising neural network, D, new samples from the noise-free distribution of $x(t = 0)$ can be generated from random noise, $x(t = T)$. This is achieved by simulating the time reversal of an ordinary differential equation defined to gradually transform examples from the data distribution, $x(t = 0)$, to random Gaussian noise, $x(t = T)$, when evolved forward in time

$$\frac{dx}{dt} = -\dot{\sigma}(t)\sigma(t)\nabla_x \log\left(p\left(x(t)\right)\right), \tag{2}$$

where the 'time' axis, t, varies from $t = 0$ (the data distribution) to $t = T$ (Gaussian noise distribution with scale σ_{max}), and $\dot{\sigma}$ is the derivative of the noise amplitude schedule with respect to the diffusion time axis (Song & Ermon, 2019; Karras et al., 2022). The term $\nabla_x \log\left(p\left(x(t)\right)\right)$ is referred to as the 'score function' or 'score network' and represents the gradient of the log-likelihood of x. The key to score-based diffusion models lies in recognizing that a well-trained de-noiser, D, can be used to approximate the score function in Equation 2 through (Karras et al., 2022)

$$\nabla_x \log\left(p\left(x(t)\right)\right) = \frac{D\left(x(t)\right) - x(t)}{\sigma(t)^2}. \tag{3}$$

Realistic (but random) ocean states, $x(t = 0)$, can thus be generated by starting with random noise, $x(t = T)$, and solving Equation 2 backward in time from $t = T$ to $t = 0$ using a finite difference discretization of the time axis and using the trained denoiser, D, to calculate the score function at each time step through Equation 3. This reverse time-stepping procedure updates the state, $x(t)$, to maximize the likelihood $p(x(t = 0))$ which is encoded in the trained score network (also referred to hereafter as the 'diffusion prior'). See S.I. Text S3 for details on how we implement D as a neural network.

2.1.2 Score-Based Data Assimilation

While reverse time-stepping Equation 2 using the trained score function (Section 2.1.1) provides a way to generate realistic ocean states, these states are random and are not related to any observations. Score-based data assimilation provides a way to control the generation process to push the generated state, $x(t = 0)$ to match the observations, y (Rozet & Louppe, 2023a). Essentially, this framework seeks to replace the score function, $\nabla_x \log\left(p\left(x(t)\right)\right)$, with the corresponding gradient of the *posterior* log-likelihood, $\nabla_x \log\left(p\left(x(t)|y\right)\right)$.

The optimal state estimate would be the one that maximizes the posterior likelihood of the reconstructed state given the available observations, $p(x|y)$, or equivalently minimizes $-\log\left(p(x|y)\right)$. The gradient of the posterior log-likelihood can be expressed through Bayes' theorem as

$$\nabla_x \log\left(p(x|y)\right) = \nabla_x \log\left(p(x)\right) + \nabla_x \log\left(p(y|x)\right), \tag{4}$$

from which it follows also that

$$\nabla_x \log\left(p(x(t)|y)\right) = \nabla_x \log\left(p(x(t))\right) + \nabla_x \log\left(p(y|x(t))\right). \tag{5}$$

Rozet and Louppe (2023a) thus propose to replace the score function in Equation 2 with the posterior log-likelihood gradient given by Equation 5. This way, when generating ocean states from random noise by simulating the time reversal of Equation 2, the final state will be one that maximizes the posterior likelihood given the observations, y, and the trained diffusion prior (i.e. the score network) which encourages the reconstructed state to 'look like' the GCM simulation training data.

At inference, the first term in Equation 5 (the score function) is known (Equation 3) and it remains to approximate the second term. This second term is formally only known at $t = 0$, i.e. the data distribution, but Rozet and Louppe (2023a) propose that, assuming a Gaussian observing process, it can be approximated by

$$p(y|x(t)) = \mathcal{N}\left(y|\mathcal{A}(\hat{x}(t)), \Sigma_y(t)\right), \tag{6}$$

where $\Sigma_y(t)$ is a heuristic variance that increases with noise level (i.e. with t), $\hat{x}(t)$ is the de-noised state predicted by the diffusion model, and $\mathcal{A}$ is the observation operator. See Rozet and Louppe (2023a) and S.I. Text S3.2 for details of the heuristic used for $\Sigma_y(t)$. While this is only an approximation of the true $p(y|x(t))$, empirically GenDA has been shown to have impressive reconstruction abilities both for idealized quasi-geostrophic turbulence (Rozet & Louppe, 2023b) and for kilometer-scale atmospheric reanalysis (Manshausen et al., 2024) in spite of using the idealized Gaussian approximation.

In summary, to generate an estimate for the ocean state from observations we start with a random state vector, $x(t = T)$, and perform reverse time steps using Equations 2, 3, 5, and 6 to sample from $p(x(t = 0)|y)$ (Figure 3). Crucially, the updates made during reverse time-stepping are not adjustments to the neural network parameters but instead updates to the state $x(t)$. This way, generated state estimates should still qualitatively 'look like' examples from the simulation since we impose our simulation-trained diffusion prior on the state estimation. In this study we propose that forcing the state estimates to be qualitatively similar to the numerical simulation will allow us to preserve fine-scale features and inter-relations between observed and unobserved variables at inference. Another advantage of the GenDA method is that it is Bayesian, so rather than producing a single state estimate, GenDA produces a distribution of plausible states sampled from the posterior distribution, achieved practically by inputting different initial random noise vectors, $x(t = T)$. The dispersion of this ensemble thus appears a natural metric of uncertainty for the resulting state estimate. In this study, we generate ensemble state estimates with 24 ensemble members and explore the suitability of ensemble dispersion for uncertainty quantification.

2.1.3 Observation Operator for Surface Ocean State Estimation

There is significant flexibility in the choice of $\mathcal{A}$ used at inference. Since a single diffusion model is trained with no specific observing system in mind, GenDA provides a natural low-cost way to use a wide variety of observing systems to produce state estimates at inference without retraining the diffusion model. Relevant types of observing systems include highly localized point-wise measurements, like from weather stations or satellite tracks, and coarse observations that represent relatively large-scale satellite footprints in space and/or time. Manshausen et al. (2024) explored sparse, point-wise measurements of the atmosphere from weather stations for $\mathcal{A}$, demonstrating the efficacy of diffusion models for inference from sparse observations. Here, we will develop a method allowing the inclusion of low-resolution state estimates to constrain the large-scale state in GenDA. The motivation for using coarse observing systems in conjunction with high-resolution sparse observations is that existing gridded satellite products for SSH, SST, and SSS (e.g. from OI) give a reasonable estimate of the ocean state at large mesoscales and above, whereas high-resolution, un-gridded satellite observations (say of SSH or SST) typically have large gaps on any given day. Incorporating these low-resolution gridded products implicitly incorporates observations from a longer time horizon to constrain the large-scale state, while sparse and instantaneous high-resolution observations will be used to inform smaller scales.

In practice, we compare low-resolution OI satellite products to the diffusion model output by coarse-graining the latter using an appropriate spatial scale. The coarse-graining scale is considered to be known for any OI product - see S.I. Text S5 for a discussion of how these coarse-graining scales can be selected. Concretely, the observation operator $\mathcal{A}$ generates several fields, including an instantaneous observation term, $\mathcal{A}_{inst}$, and low-resolution satellite product terms for each of the OI product, $\mathcal{A}_{smooth}$:

$$\mathcal{A}(x) = \mathrm{concat}(\mathcal{A}_{inst}(x), \mathcal{A}_{smooth}(x; \sigma)). \tag{7}$$

$\mathcal{A}_{inst}(x)$ selects the indices for the nearest pixels and variables (channels) where instantaneous observations are available and will therefore yield sparse, high-resolution satellite observations of SSH or SST. Meanwhile, $\mathcal{A}_{smooth}(x; \sigma)$ is a coarse-graining operation, where we apply a low-pass Gaussian filter with kernel width, σ, to the state estimate, x. This allows us to compare a coarse-grained view of the state estimate to a low-resolution satellite product to encourage agreement at large scales without penalizing small-scale features below the resolution limit of the low-resolution satellite products. We apply $\mathcal{A}_{smooth}(x;\sigma)$ to all variables for which we have access to low-resolution real-world satellite products (i.e. SSH, SST, SSS) and we choose coarse-graining scales, σ, for each variable to be representative of the effective resolution of the respective satellite products. Note that the coarse-graining scale, σ, applied to each satellite observable in the observation operator is something we prescribe and should be chosen to reflect the effective resolution of each satellite product being assimilated (S.I. Text S5). We treat ageostrophic current velocities as being essentially unobserved in the real world, and so neither $\mathcal{A}_{inst}(x)$ nor $\mathcal{A}_{smooth}(x;\sigma)$ returns any values for u_{ageo} or v_{ageo}.

In practice, we find that a significant portion of the ageostrophic surface currents is driven by wind stress. This poses a problem for reconstructing ageostrophic currents from only SSH, SST, and SSS observations without information about the wind-forcing. We employ two strategies to mitigate this. Firstly, we use a linear Ekman model (S.I. Text S1) to predict the wind-driven surface currents, u_{Ek} and v_{Ek}, from the wind stress and subtract this from u_{ageo} and v_{ageo}, re-framing our state estimation problem so that we seek to estimate

$$u_{ageo} = u_{total} - u_{geo} - u_{Ek}, \tag{8}$$

and

$$v_{ageo} = v_{total} - v_{geo} - v_{Ek}. \tag{9}$$

Secondly, since the linear Ekman model doesn't capture all wind-driven variability in surface currents, we also expand our state vector, x, to include surface winds, u_{atmos} and v_{atmos}. We thus train the diffusion model to jointly generate surface ocean states alongside corresponding surface wind fields. During the assimilation process, we then provide surface wind 'observations' through $\mathcal{A}_{inst}(x)$, providing information about the wind-forcing to the state estimation and thus improving the reconstruction of ageostrophic surface currents (S.I. Text S2). Note, this method is still directly applicable to real-world observations since reanalysis winds (e.g. ERA5) are available in the real-world setting.

2.2 UNet Regression: Baseline Supervised Learning Framework

To provide a baseline method against which to compare and contrast the GenDA state estimates we also implement a supervised learning approach. Unlike GenDA, this supervised approach is trained specifically for the observing system under consideration by creating pseudo-observations from the high-resolution GCM simulation and training a neural network to predict the corresponding state vector, x, in one shot from these inputs. That is, we estimate the state vector as

$$\hat{x} = f_\theta(y), \tag{10}$$

where $\hat{x}$ is our estimate of x, y are the potentially sparse or degraded observations, and f_θ is a neural network whose parameters, θ, we seek to optimize by minimizing the MSE between $\hat{x}$ and x. Note, unlike GenDA the supervised approach provides a single prediction for each state rather than a distribution and requires bespoke training for each observing system.

In practice, we implement f_θ as a UNet (Ronneberger et al., 2015) (S.I. Text S3) with 7 input channels in y:

- Simulated sparse, high-resolution (i.e. 'Level 3' or L3) SSH satellite observations
- Simulated sparse, high-resolution (i.e. 'Level 3' or L3) SST satellite observations
- Zonal surface wind from reanalysis
- Meridional surface wind from reanalysis
- Simulated low-resolution, gap-free (i.e. 'Level 4' or L4) SSH from OI

- Simulated low-resolution, gap-free (i.e. 'Level 4' or L4) SST from OI
- Simulated low-resolution, gap-free (i.e. 'Level 4' or L4) SSS from OI

Hereafter we refer to the baseline supervised learning method as 'UNet Regression'.

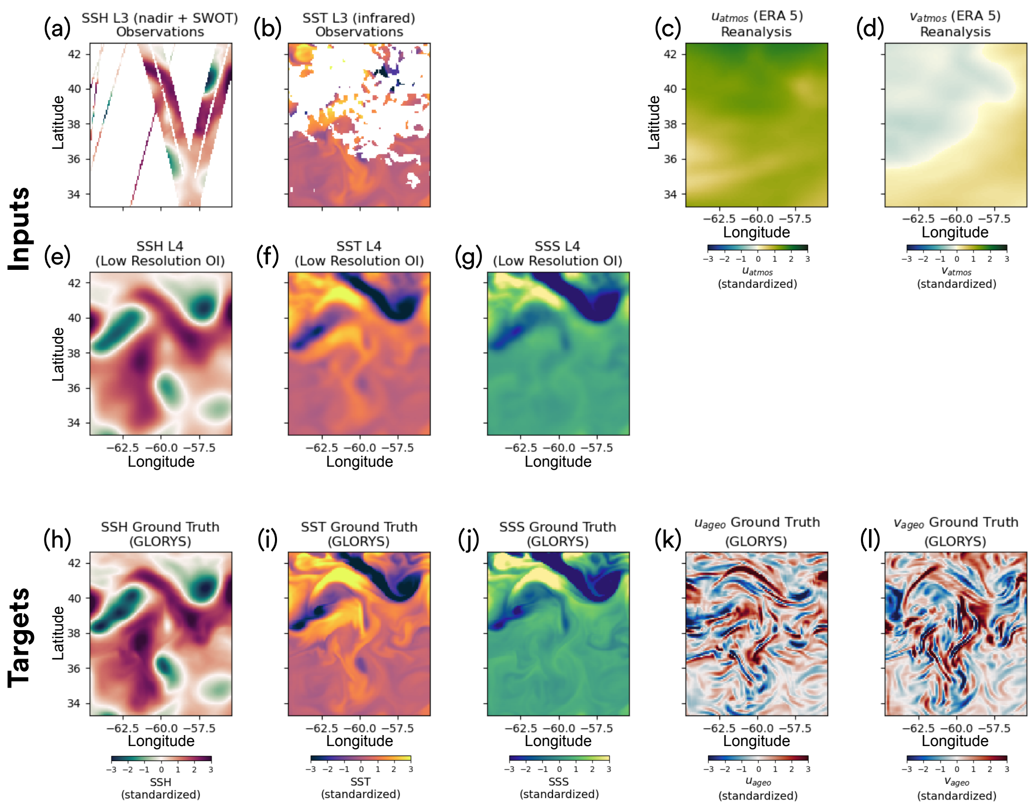

Figure 4. Example inputs and targets for multi-modal surface ocean state estimation simulated from GLORYS re-analysis product in our observing system simulation experiment (Section 3.2). The inputs are (a) simulated L3 SSH observations from a constellation of nadir altimeters and SWOT, (b) cloud-obscured L3 SST observations from infrared radiometers, (c) & (d) surface winds from ERA 5 (Section 2.1), (e)-(g) coarse-grained SSH, SST, and SSS to simulate existing low-resolution satellite products from OI. The target variables are the gap-free, high-resolution (h) SSH, (i) SST, (j) SSS, (k) & (l) ageostrophic surface currents. Ageostrophic currents are not observed by satellites. All values are standardized (Section 3.1).

3 Datasets & Experiment Set-Up

3.1 Oceanic & Atmospheric Reanalysis Products for Training and Evaluation

In this study, we provide a regional proof-of-concept of eddy-resolving surface ocean state estimation by training GenDA on data from a high-resolution reanalysis product, GLORYS 12 (Lellouche et al., 2021; E.U. Copernicus Marine Service Information (CMEMS), 2024d). This product is developed by assimilating satellite and in situ observations into the NEMO ocean GCM with 1/12° grid resolution using a reduced-order Kalman filter. The ocean GCM is driven at the surface by atmospheric forcing from the ECMWF Reanalysis product, commonly known as ERA 5 (Copernicus Climate Change Service (C3S, 2024; Hersbach et al., 2020). GLORYS 12 does not resolve submesoscale dynamics which is a key driver of ocean eddy dynamics, however, it has a sufficiently fine grid to resolve mesoscale baroclinic instability (a key formation mechanism for mesoscale eddies) and exhibits an abundance of submesoscale fronts and filaments generated by a forward cascade of enstrophy by mesoscale eddy stirring. We hence consider it a sufficiently realistic and high-resolution test bed for the GenDA method, though we emphasize that in the future, GenDA can be trained on free-running submesoscale-resolving simulations (e.g. LLC 4320 (Su et al., 2018)). One of the motivations of this study is that data assimilation products like GLORYS currently show large errors when compared to satellite observations at mesoscales, suggesting that optimizing the full 3D state of the ocean and ensuring its conformity to dynamical equations of motion comes at the expense of accurately placing mesoscale eddies and fronts at the surface. We hypothesize that GenDA, by optimizing only the surface fields, will reduce these biases while preserving a substantial amount of physical characteristics of the GLORYS 12 fields seen during training through the diffusion prior.

The experiments presented in this study focus on the Gulf Stream Extension region (55-65° W, 33-43° N) which has one of the most energetic eddy fields in the global ocean. Focusing on this region also allows easy comparison to a number of other machine learning applications for SSH mapping through an Ocean Data Challenge (Ballarotta et al., 2021; Metref et al., 2023). A wider region of (70-40° W, 25-45° N) is used for all neural network training. The years 2010-2016 are used for network training, 2018-2020 for cross-validation, and 2017 is withheld as an independent test year on which the evaluation metrics presented throughout the rest of the study are calculated.

All variables in the 7-variable state vector, x = (SSH, SST, SSS, u_{ageo}, v_{ageo}, u_{atmos}, v_{atmos}), are standardized by subtracting the mean and dividing by the standard deviation of each variable calculated over the full training domain and time-series. In the case of SST and SSS, the strong seasonal cycle is removed by subtracting a monthly climatology rather than the mean. The ageostrophic surface currents are taken at 15 m depth to be more reflective of the eddy-driven ocean currents than those at the surface layer. For both GenDA and the UNet Regression baseline, the state vector, x, is estimated on a regular latitude-longitude grid at the same 1/12° resolution as GLORYS 12 with dimensions of 128 by 128, corresponding roughly to a domain of size 1000 km.

3.2 Experiment 1: Observing System Simulation Experiment (OSSE)

First, we assess GenDA's reconstruction abilities in a controlled environment where we have access to the full ground-truth fields for validation through an observing system simulation experiment (OSSE). After training GenDA on GLORYS data from 2010-2016, we generate synthetic satellite observations of GLORYS using the withheld testing year 2017 and evaluate GenDA's ability to reconstruct the full fields, including variables unobserved by satellites (Figure 4).

3.2.1 Generation of Simulated L3 Satellite Observations

In this OSSE we consider two different sources of Level 3 (L3) input observations: SSH from satellite altimeters and high-resolution SST from satellite infrared radiometers. L3 refers to observations before they have been interpolated to a full gridded field, so L3 observations are sparse but high-resolution.

We generate synthetic L3 SSH observations by sub-sampling the GLORYS SSH field along the observation tracks from all conventional nadir altimeters available in the year 2017: SARAL/Altika, Jason 2, Jason 3, Sentinel 3A, Haiyang-2A and Cryosat-2. Nadir altimeters provide point-wise SSH measurements beneath the satellite track with an along-track spacing of approximately 7 km. In addition, we assess the impact of including wide-swath observations from the recently-launched Surface Water and Ocean Topography (SWOT) mission which provides two 60 km wide swaths of SSH measurements at 2 km resolution with a narrow gap between the swaths (Fu et al., 2024). While SWOT has high spatial sampling it has a relatively long orbit repeat of 21 days. We sub-sample GLORYS SSH at the locations of SWOT observations by repeating its 21-day science orbit throughout the year 2017.

Satellite infrared radiometers observe SST at kilometer resolution but there are large gaps due to cloud cover. Here, we sub-sample GLORYS SST using cloud masks from the ODYSSEA SST Multi-Sensor L3 product (E.U. Copernicus Marine Service Information (CMEMS), 2024a). This ensures the applied cloud cover is realistic, with cloud cover varying on any given day between near-complete occlusion and cloud-free conditions. For both SSH and SST L3 observations we add Gaussian noise with amplitude chosen to reflect the noise for each sensor. We take the SSH noise amplitude from the relevant CMEMS product (E.U. Copernicus Marine Service Information (CMEMS), 2024c) and for SST from the average of the error estimates provided in the ODYSSEA SST Multi-Sensor L3 product (E.U. Copernicus Marine Service Information (CMEMS), 2024a).

3.2.2 Generation of Simulated L4 Satellite Products

In addition to high-resolution L3 observations, we provide simulated low-resolution gridded (‘Level 4’, L4) products for SSH, SST, and SSS. L4 refers to observations that have been interpolated to a full gridded field (typically using OI), so L4 observations are gap-free but low-resolution.

The interpolation algorithms used to interpolate between observations smooth out small-scale features, providing spatio-temporally coarse-grained estimates of the real fields. We simulate this by coarse-graining the GLORYS SSH, SST, and SSS both in space and time using a Gaussian kernel with spatial and temporal widths selected to be roughly representative of the resolutions of available L4 products (S.I. Text S5 & Table S2). These coarse-grained fields are then compared to coarse-grained output from GenDA in the observation operator when minimizing the reconstruction loss at inference. Since GenDA is applied only on single temporal snapshots, we can’t replicate the temporal coarse-graining in the L4 products in the GenDA observation operator, and so resort to only coarse-graining in space. Finally, we also provide gridded values for u_{atmos} and v_{atmos} from ERA 5 with no additional coarse-graining applied since this product would also be available to use in the real-world setting.

Taken together, the simulated observations provided to GenDA and UNet Regression are:

- Along-track L3 SSH from a constellation of nadir altimeters
- Wide-swath L3 SSH from SWOT
- Cloud-obscured high-resolution L3 SST
- Coarse-grained L4 SSH
- Coarse-grained L4 SST
- Coarse-grained L4 SSS
- Surface wind velocities from ERA 5

Note, no observations are provided for u_{ageo} or v_{ageo} since these are not typically observed in the real world so we reconstruct these in an unsupervised manner.

3.2.3 Evaluation Metrics

We evaluate the point-wise accuracy for each reconstructed variable using the coefficient of determination (R^2), which represents the fraction of variance explained. For

SSH and SST, we remove any pixels provided as part of the L3 observations from the evaluation metrics. Since the simulated low-resolution L4 OI products for SSH, SST, and SSS already capture a significant part of the signal, we also present R^2 for SSH, SST, and SSS calculated on the residual from the low-resolution L4 products. Note that R^2 is by definition zero for the L4 OI predictions in this setting and any positive value represents an improvement over OI. We assess the impact of cloud-free L3 SST observations on the reconstruction accuracy by computing R^2 separately for pixels that are clouded and un-clouded respectively. Since the average cloud cover has a significant spatial structure, we randomly over-sample and under-sample the clouded and un-clouded pixels using weights that ensure both datasets are uniformly drawn in latitude-longitude (See S.I. Text S6). We use the same procedure to assess the impact of L3 SWOT SSH observations on reconstruction accuracy.

We also evaluate the wavenumber spectra of each reconstructed variable and compare them to the ground truth from GLORYS. All spectra in this manuscript are calculated by estimating the 2D power spectral densities for each time step, averaging in time, then averaging azimuthally. Note, u_{ageo} and v_{ageo} are evaluated jointly through the ageostrophic kinetic energy spectrum and we also derive the geostrophic kinetic energy spectrum from the SSH reconstructions. Since we focus here on multi-modal state estimation, we also evaluate the spectra of eddy temperature, F_T, and salt, F_S, fluxes which are sensitive to the resolution of both velocity and SST/SSS and are crucial diagnostics of the impacts of ocean eddies on climate. We focus here on the meridional eddy fluxes since these induce significant transport across the Gulf Stream in our test region,

$$F_T = v'\mathrm{SST}', \tag{11}$$
$$F_S = v'\mathrm{SSS}', \tag{12}$$

where primed quantities denote deviations from monthly climatology (Guo et al., 2022).

We also consider higher-order diagnostics of eddy dynamics that can be derived from SSH, namely the geostrophic Okubo-Weiss quantity, W, (Okubo, 1970; Weiss, 1991) which delineates strain-dominated flows from vorticity-dominated flows

$$W = (\sigma^2 - \zeta^2) = (\sigma_n^2 + \sigma_s^2 - \zeta^2), \tag{13}$$

where

$$\sigma = \sqrt{\sigma_n^2 + \sigma_s^2} = \sqrt{\left(\frac{\partial u}{\partial x} - \frac{\partial v}{\partial y}\right)^2 + \left(\frac{\partial v}{\partial x} + \frac{\partial u}{\partial y}\right)^2} \tag{14}$$

is the strain rate and

$$\zeta = \frac{\partial v}{\partial x} - \frac{\partial u}{\partial y} \tag{15}$$

is the relative vorticity. We further explore the accuracy of diagnosed eddy dynamics by evaluating the joint probability density function (JPDF) of σ and ζ for each reconstruction. The accuracy of these diagnostics of eddy dynamics is important for studies of ocean scale interactions and are highly sensitive to the accuracy and resolution of SSH (Martin et al., 2023, 2024b).

Finally, we evaluate the suitability of GenDA ensemble dispersion for uncertainty quantification through a rank histogram as is widely used in probabilistic weather forecasting (Talagrand, 1999). This shows the probability that the ground truth falls in each rank of the ordered ensemble of predictions. Hence, a well-calibrated ensemble would have a flat rank histogram, an under-dispersive ensemble would have a ‘u-shaped’ rank histogram, an over-dispersive ensemble would have a ‘n-shaped’ rank histogram, and a biased ensemble would have an asymmetric rank histogram.

3.3 Experiment 2: Observing System Experiment (OSE)

To assess the ability of GenDA to generalize to the real-world ocean, we also perform an observing system experiment (OSE) in which we construct state estimates from real-world satellite observations. This poses a more stringent test of the method since now the observations come from the real-world ocean which potentially exhibits different characteristics to the GLORYS 12 simulated fields. Applying GenDA in the real world is akin to data assimilation, where we seek a field that qualitatively preserves the characteristics of GLORYS but that best matches available observations. Since GLORYS itself is already assimilated to observations, we can use errors against real-world satellite observations to benchmark GenDA against this state-of-the-art data assimilation product.

We conduct our OSE in the same Gulf Stream Extension region (55-65° W, 33-43° N) as in the OSSE, again for the withheld test year 2017.

3.3.1 L3 Satellite Observations

We provide L3 observations of both SSH and SST. For SSH, the observations come from a constellation of nadir altimeters (SARAL/Altika, Jason 2, Jason 3, Sentinel 3A, Haiyang-2A) (E.U. Copernicus Marine Service Information (CMEMS), 2024b). SWOT was yet to be launched during this test year so we provide only along-track SSH observations. To independently evaluate the accuracy of the mapped SSH fields, we withhold one altimeter, CryoSat-2, at inference and use this withheld altimeter as a ground truth for the mapped SSH. This follows the configuration of the 2021a Ocean Data Challenge (Ballarotta et al., 2021), allowing us to benchmark the performance of GenDA on real-world observations against state-of-the-art SSH mapping methods. For SST, we provide cloud-occluded infrared radiometer observations from the ODYSSEA multi-satellite product (E.U. Copernicus Marine Service Information (CMEMS), 2024a). This product collates SST observations from a range of different satellites onto a regular 0.1° grid and includes only nighttime observations to remove diurnal variability.

3.3.2 L4 Satellite Products

We also provide low-resolution L4 estimates of SSH, SST, and SSS. For SSH, we use output from the deep learning model, ConvLSTM, presented in Martin et al. (2023). This method uses a supervised, observation-only learning regression approach to estimate gridded SSH at higher resolution than can be achieved with OI by synthesizing along-track SSH and gridded SST. In order to preserve the independence of the withheld evaluation altimeter, CryoSat-2, we ensure that the L4 SSH product was generated using all apart from the withheld altimeter and the network was never trained on observations from 2017. The ConvLSTM SSH fields have an effective resolution of 100 km (S.I. Table S3 in Martin et al. (2024b)).

For SST, we use the REMSS MW-OI Global Foundation Sea Surface Temperature analysis product (Remote Sensing Systems, 2017). This product uses OI to interpolate observations from microwave radiometer sensors onboard multiple satellites into a gridded L4 SST estimate. Note microwave radiometers have lower spatial resolution than the infrared observations we use for L3, but these sensors can penetrate clouds. The product is provided on a 1/4° grid and we linearly interpolate it to the GenDA grid.

For SSS, we use the CMEMS Multi Observation Global Ocean Sea Surface Salinity and Sea Surface Density product (E.U. Copernicus Marine Service Information (CMEMS), 2024e). This product is obtained through a multivariate OI algorithm that combines SSS images from multiple satellites with in situ salinity measurements and satellite SST and is provided on a 1/8° grid which we linearly interpolate to the GenDA grid.

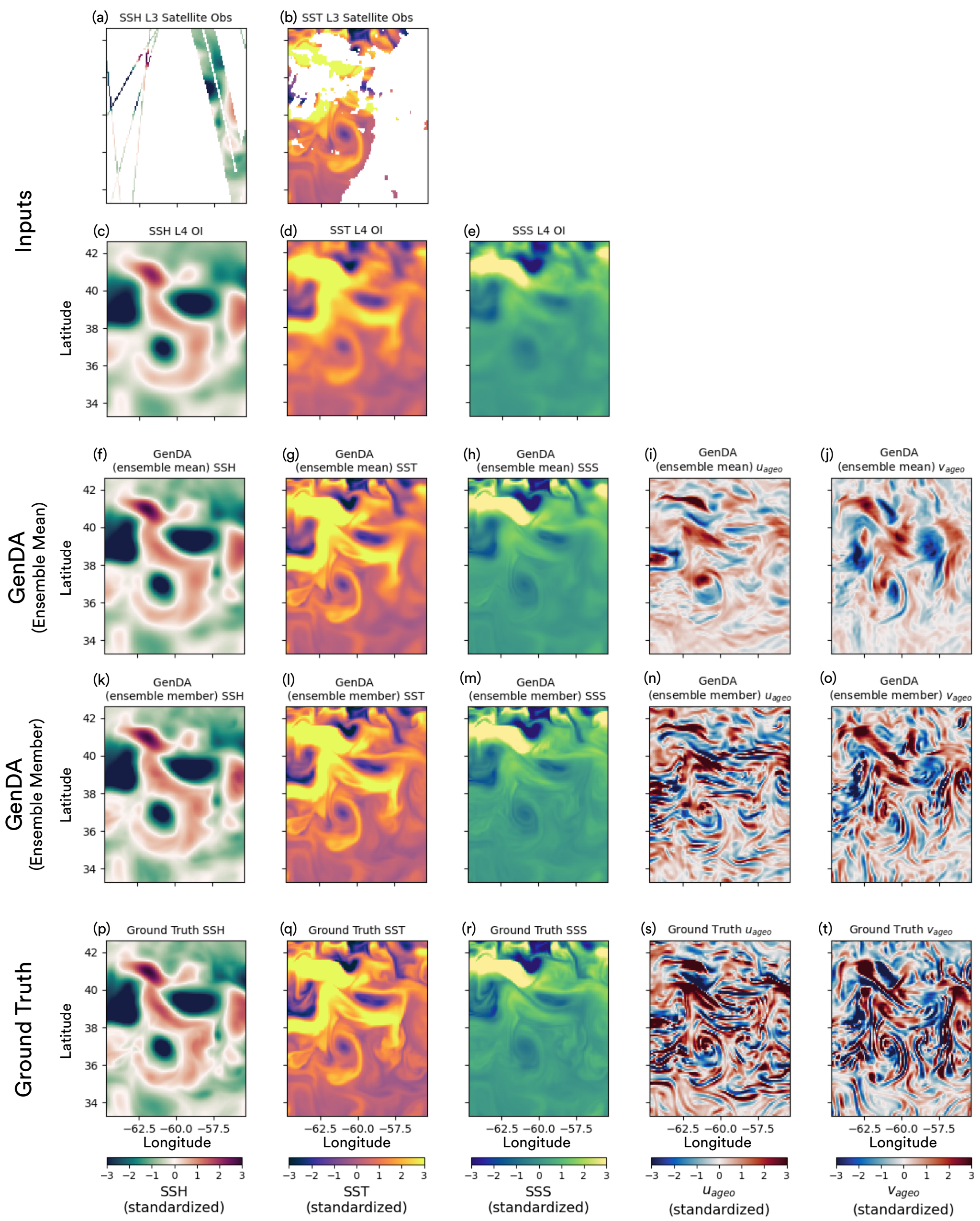

Figure 5. Example GenDA OSSE prediction for 2017-04-27 (See S.I. Movie S1 for all dates). First row, input L3 observations assimilated: (a) SSH & (b) SST. Second row, input low-resolution L4 satellite products assimilated: (c) SSH, (d) SST, & (e) SSS. Third row, GenDA ensemble mean predictions for (f) SSH, (g) SST, (h) SSS, (i) u_{ageo}, and (j) v_{ageo}. Fourth row, (k)-(o) GenDA ensemble member predictions. Fifth row, (p)-(t) ground truth fields (GLORYS). Note ERA 5 surface winds are also provided as input and predicted by GenDA but are not plotted since they match almost exactly.

The effective coarse-graining scales of the real-world L4 SSH, SST, and SSS products are not known a priori, raising the question of what coarse-graining scales, σ, to prescribe in the GenDA observation operator. We choose coarse-graining scales (S.I. Table S3) based on an a posteriori tuning strategy described in S.I. Text S5.2, though we acknowledge this choice is ultimately somewhat subjective.

As in the OSSE (Section 3.2), we also provide atmospheric wind speeds from ERA 5. No observations are provided of ageostrophic surface currents and these are reconstructed in an unsupervised manner.

In sum, GenDA and the UNet Regression are provided:

- L3 along-track SSH from 5 nadir altimeters
- L3 infrared SST observations occluded by clouds
- Coarse L4 SSH from ConvLSTM
- Coarse L4 SST from REMSS MW-OI product
- Coarse L4 SSS from CMEMS Multi-Obs product
- Surface wind velocities from ERA 5

3.3.3 Evaluation Metrics

We evaluate the mapped SSH fields along-track using the independent withheld satellite altimeter, CryoSat-2, through the metrics provided in Ocean Data Challenge 2021a (Ballarotta et al., 2021). Specifically, we evaluate the 'RMSE score', μ, and the annual standard deviation of its daily mean, σ, where

$$\mu = 1 - \frac{\mathrm{RMSE}(\eta_{pred}, \eta_{observed})}{\mathrm{RMS}(\eta_{observed})} \tag{16}$$

and η is the SSH. We also estimate the 'effective resolution' of the SSH maps by finding the wavelength at which the signal-to-error ratio of the maps crosses a threshold in spectral space when compared to along-track segments of SSH from CryoSat-2 following the methodology of Ballarotta et al. (2019). We stress that the effective resolution evaluates both the magnitude and phase of the SSH spectrum. This is different to identifying a wavelength below which the magnitude of the spectrum rolls off due to smoothing. Thus, a state estimate can show significant amplitude at small scales below the effective resolution (e.g. with a power law inertial range spectrum) but these scales are not counted as 'resolved' since their phase is not reliably estimated.

To evaluate the SST, we artificially apply additional clouds to the L3 SST observations by randomly shuffling the cloud masks between days and applying the shuffled cloud mask on top of the already-cloudy L3 SST. We then calculate R^2 against the L3 SST using only the pixels that were masked out by the additional cloud masking.

Finally, we compute the dynamical diagnostics outlined in Section 3.2.3 to test if GenDA preserves the dynamical characteristics of GLORYS when applied in the real world.

4 Results

Since the focus of this study is state estimation from observations, we here focus only on the results of applying our trained diffusion prior, D, to state estimation through GenDA. The reader is referred to S.I. Text S4 for the results of training D to de-noise GLORYS 12 ocean states. After being trained on 10 million ocean state vectors, requiring 72 NVIDIA V100 GPU-hours, D can skillfully generate realistic ocean states resembling the GLORYS training data (S.I. Text S4, Figures S1 & S2). We now proceed to evaluate GenDA's state estimation capabilities.

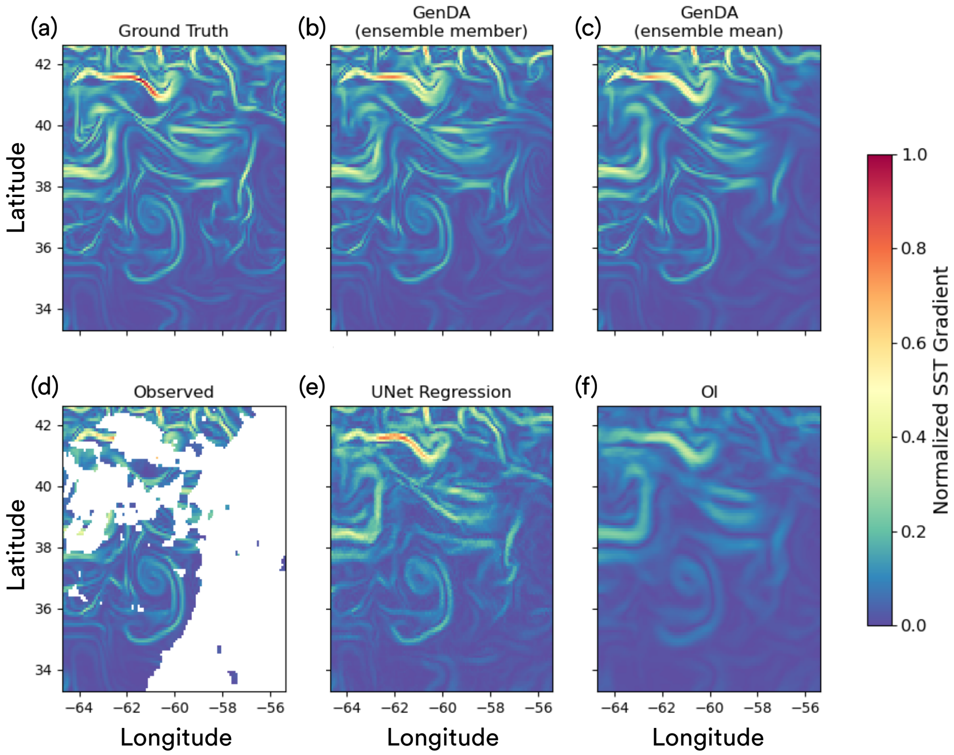

Figure 6. Magnitude of SST gradient, normalized by dividing by the maximum ground truth SST gradient, from (a) ground truth target field from GLORYS, (b) GenDA ensemble member prediction, (c) GenDA ensemble mean prediction, (d) cloud-obscured L3 SST observations assimilated, (e) UNet Regression, and (f) the coarse-grained L4 'OI' input assimilated.

4.1 Experiment 1 (OSSE): Performance on Simulated Satellite Observations

4.1.1 Point-wise Accuracy of Predictions

After being assimilated to the simulated L3 and L4 observations (Figure 5a-e), GenDA predictions (Figure 5f-o) appear to visually match the GLORYS ground truth closely (Figure 5p-t). At large scales, the SSH, SST, and SSS predictions match those from the low-resolution L4 observations (panels c-e) both in the ensemble mean (panels f-h) and for an individual ensemble member (panels k-m). At smaller scales, the predictions appear to resolve additional fine-scale features missing in the low-resolution L4 inputs. Where high-resolution L3 SSH and SST observations (panels a & b) were assimilated, both the ensemble mean (panels f & g) and ensemble member (panels k & l) predictions match the observations even at small scales. In contrast, where L3 observations are not available, the ensemble mean predictions smooth out small-scale frontal features compared to the ground truth (panels p & q). The ensemble member predictions (panels k & l) do contain frontal features throughout the domain, albeit with less point-wise agreement to the ground truth in the absence of L3 observations. Despite only assimilating low-resolution L4 SSS (panel e), the ensemble mean and ensemble members (panels h & m) exhibit fine-scale frontal SSS features. The ensemble mean SSS frontal features (panel h) appear to be smoothed out where L3 SST observations weren't available (panel b), emphasizing the close relationship between SST and SSS and suggesting small-scale SSS is largely predictable from L3 SST using GenDA.

Remarkably, despite no observations of ageostrophic surface currents being assimilated, GenDA captures many of the features in the ageostrophic surface current field (compare panels i, j, n, & o to s & t). For surface currents, a clear difference emerges between the ensemble mean (panels i & j) and the ensemble member (panels n & o). The ensemble member exhibits fine-scale frontal jets with variance comparable to the ground truth, though the point-wise agreement to the ground truth for these jets appears mixed. Meanwhile, the ensemble mean exhibits lower variance and only the larger, eddy-driven currents remain. This suggests a higher degree of confidence in the predictions for the large-scale eddy-driven ageostrophic currents, which are largely due to cyclogeostrophic balance (Penven et al., 2014; Cao et al., 2023), while each ensemble member produces fine-scale frontal jets that vary in location and hence average out in the ensemble mean.

The distinction between the ensemble mean and ensemble member is further emphasized in Figure 6 by evaluating the magnitude of SST gradients. Despite the Eastern side of the domain being entirely obscured by clouds (panel d), the GenDA ensemble member (panel b) predicts a series of fine-scale SST fronts whereas the ensemble mean (panel c) predicts broader, weaker fronts reflecting the uncertainty in the location of each front. Note the UNet Regression (panel e) fronts in the cloud-obscured region are qualitatively similar to those in the GenDA ensemble mean, reflecting that the regression formulation leads it to predict the mean of the distribution, smoothing out smaller scales. Both the UNet Regression and GenDA ensemble mean have sharper fronts than those from OI (panel f).

When evaluated over the full withheld testing year, both GenDA and UNet Regression are able to reconstruct SSH, SST, and SSS with higher R^2 than the low-resolution L4 OI (Table 1). The GenDA ensemble mean outperforms the ensemble member on these point-wise accuracy metrics, emphasizing that the ensemble provides a more accurate prediction than any individual ensemble member at the expense of smoothing out fine-scale features. UNet Regression outperforms GenDA in terms of point-wise accuracy across all variables, though only marginally for SSH, SST, and SSS compared to the GenDA ensemble mean. This suggests that bespoke training for the considered observing system, and optimization of regression metrics (i.e. MSE) in the UNet Regression loss function, allows UNet Regression to learn a more accurate mapping than the more general GenDA framework, especially for the unobserved ageostrophic surface currents. However, we will show below that the advantages of GenDA become apparent when it is applied to real-world observations and when evaluating the physical consistency across scales of the reconstructions.

R^2 for each variable							
Method	SSH	SST	SSS	u_{ageo}	v_{ageo}	ζ_{geo}	ζ_{ageo}
Low Resolution L4 (OI)	0.969 (0.00)	0.923 (0.00)	0.903 (0.00)	n/a	n/a	0.530	n/a
Supervised UNet Regression	0.992 (0.748)	0.964 (0.529)	0.963 (0.623)	0.617	0.591	0.732*	0.436
GenDA (ensemble mean)	0.991 (0.695)	0.957 (0.444)	0.962 (0.608)	0.383	0.369	0.721	0.177
GenDA (ensemble member)	0.987 (0.598)	0.941 (0.241)	0.949 (0.473)	0.017	0.011	0.564	-0.287

Table 1: Coefficient of determination, R^2, for each variable and reconstruction methods, higher values closer to 1 indicate more accurate predictions. Values in brackets for SSH, SST, and SSS are R^2 calculated on the residual from the low resolution L4 OI inputs, so any positive value indicates an improvement over OI. Ageostrophic currents and vorticity are not retrievable from the low-resolution L4 OI method since this only estimates satellite observables. The asterisk for UNet Regression geostrophic vorticity indicates that the field was smoothed using a Gaussian filter with a sigma of 1 pixel before calculating SSH gradients to remove high-frequency checkerboard artifacts, improving R^2 for ζ_{geo}.

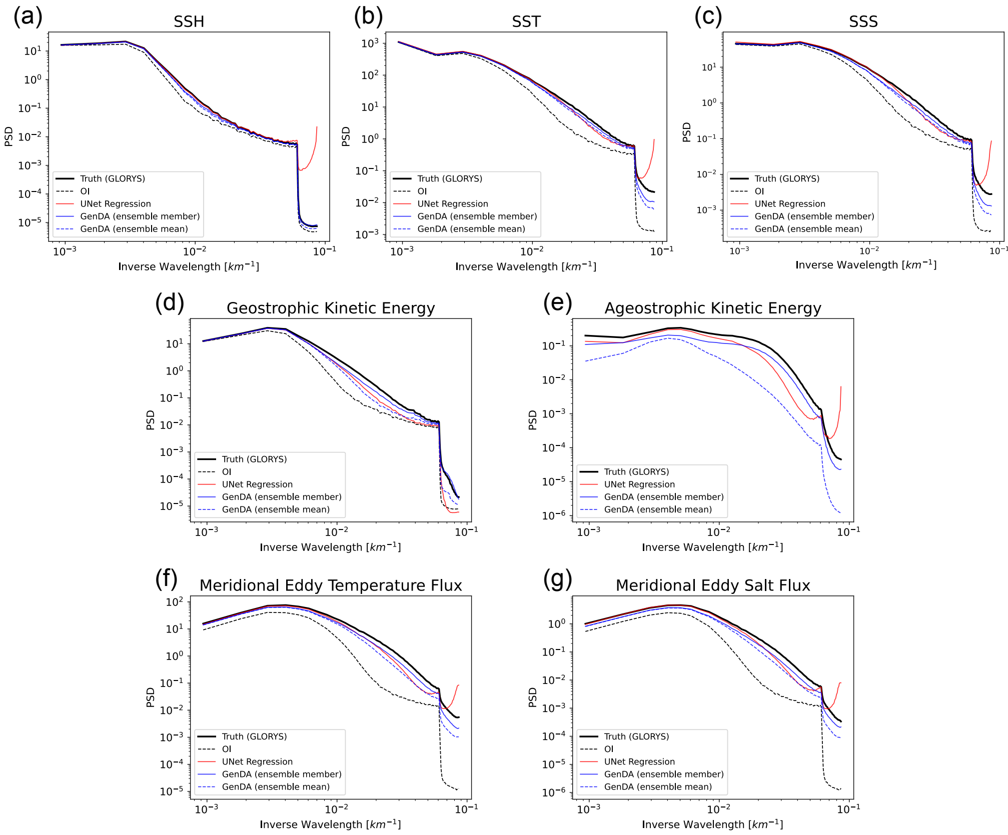

Figure 7. Spectra for (a) SSH, (b) SST, (c) SSS, (d) geostrophic kinetic energy, (e) ageostrophic kinetic energy, (f) meridional eddy temperature flux, and (g) meridional eddy salt flux. (solid black) ground truth target field from GLORYS, (dashed black) low resolution L4 OI input assimilated, (solid red) UNet Regression, (solid blue) GenDA ensemble member, and (dashed blue) GenDA ensemble mean.

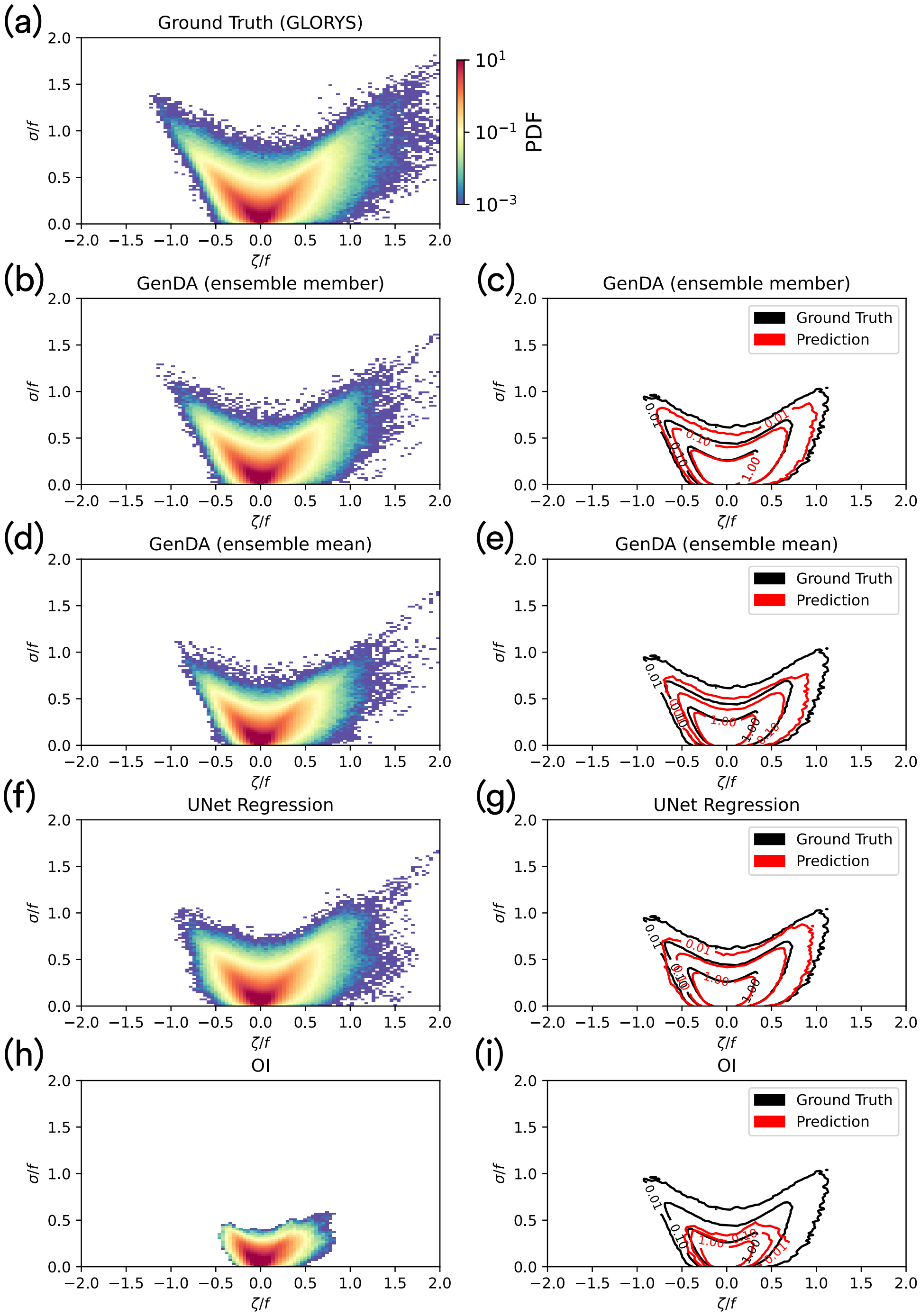

Figure 8. Geostrophic joint vorticity-strain probability density functions for (a) ground truth (GLORYS), (b), GenDA (ensemble member), (d) GenDA (ensemble mean), (f) UNet Regression, and (h) OI. Right panels show a comparison between the ground truth (black) and predicted (red) JPDFs at three logarithmically spaced contour levels for (c) GenDA (ensemble member), (e) GenDA (ensemble mean), (g) UNet Regression, and (i) OI.

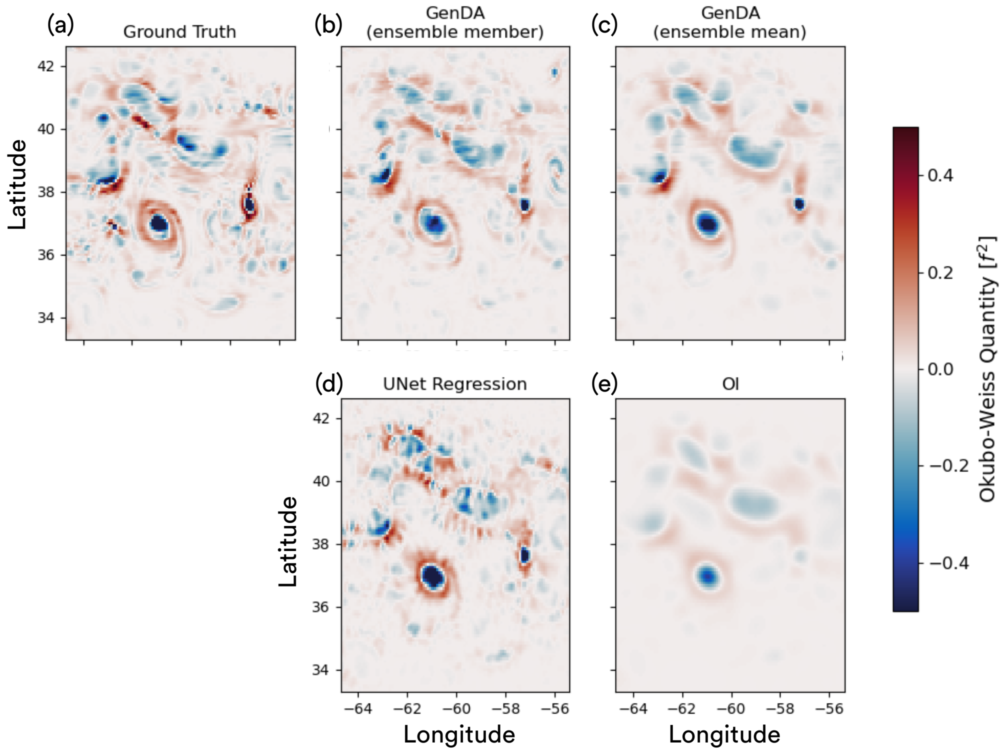

Figure 9. Geostrophic Okubo-Weiss quantity for (a) ground truth target field from GLORYS, (b) GenDA ensemble memner, (c) GenDA ensemble mean, (d) UNet Regression, and (e) OI. Negative values indicate vorticity dominates (as in eddy cores) whereas positive values show where strain dominates (as around eddy peripheries).

4.1.2 Spectral Evaluation & Eddy Dynamics

Evaluating the spectra for the satellite observables (SSH, SST, and SSS) highlights the fact that both GenDA and UNet Regression preserve more fine-scale features than the low resolution L4 OI, with spectra closer to the ground truth GLORYS fields (Figure 7a-c). In all cases, UNet Regression appears to better estimate the variance at large scales than GenDA, which likely drives the improvement in R^2 seen in Table 1. However, for SST and SSS UNet Regression shows a spectral roll-off, underestimating variance at smaller scales with an overly-steep spectral slope compared to the ground truth. By contrast, the GenDA reconstructions show shallow spectral slopes, more like those in the ground truth data, albeit with the GenDA ensemble mean spectral slope beginning to steepen below 100 km. The fact that GenDA ensemble member reconstructions show similar spectral slopes to the ground-truth fields across all scales highlights the ability of the diffusion prior to ensure reconstructions retain the physical characteristics of the GLORYS training data across scales. At smaller scales, the UNet Regression spectra flatten due to the appearance of high-frequency ‘checkerboard’ artifacts in the predictions which in the case of SSH overwhelm the signal below 40 km. Such artifacts don’t appear in the GenDA reconstructions likely due to its different training objective (i.e. de-noising).

Considering the kinetic energy spectra of the unobserved ageostrophic currents (Figure 7e), UNet Regression appears to better capture the variance at large scales, possibly indicating that GenDA is not optimal for reconstructing large-scale wind-driven surface currents that remain after subtracting the linear Ekman currents. However, UNet Regression again exhibits an overly-steep spectral slope at scales below 100 km where the regression formulation begins to smooth out fine-scale frontal jets. The GenDA ensemble member matches the ground truth spectrum more closely all the way down to the grid resolution. By contrast, the GenDA ensemble mean strongly under-estimates variance below 100 km, consistent with the smooth ensemble mean in Figure 5i,j. A similar picture emerges when considering the geostrophic kinetic energy spectra (Figure 7d), with the GenDA ensemble member coming closest to the ground truth spectra albeit still underestimating the variance at all scales. This emphasizes the advantage of GenDA's generative formulation for reconstructing higher-order dynamical diagnostics which are sensitive to the smoothing of SSH (geostrophic kinetic energy goes as the square of the gradient of SSH). Finally, the spectra of the eddy temperature and salt fluxes (Figure 7f & g respectively) show how the smoothing of SSH and SST/SSS compound in the low-resolution OI reconstructions, leading to a severe under-estimation of small-scale eddy fluxes. In contrast, GenDA ensemble member fluxes have a similar spectral slope to the ground truth all the way down to the grid resolution.

The ability of GenDA ensemble members to reconstruct realistic-looking eddy dynamics is further illustrated by comparing the geostrophic vorticity-strain JPDF to that calculated from the GLORYS ground truth SSH (Figure 8). Compared to the ensemble mean or UNet Regression, GenDA ensemble members better capture the long tails in the vorticity and strain distributions. The improved reconstruction of vorticity and strain can also be observed visually for a snapshot through the Okubo-Weiss quantity (Figure 9). Accurately reconstructing geostrophic vorticity and strain, reflected in both the JPDF and the Okubo-Weiss quantity, is vital for studies of ocean eddy dynamics since they are necessary to diagnose ageostrophic dynamics, vertical velocities, frontogenesis rates, and kinetic energy cascades between scales.

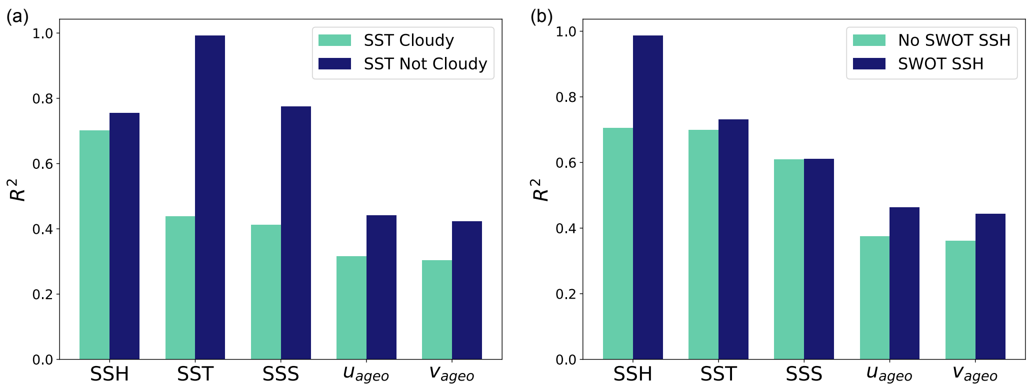

Figure 10. R^2 for GenDA ensemble mean OSSE predictions split by (a) whether cloud-free L3 SST observations were (dark blue) available or (teal) unavailable and (b) whether SWOT L3 SSH observations were (dark blue) available or (teal) unavailable. R^2 values for SSH, SST, and SSS were calculated on the residual from the OI predictions, so any positive value indicates an improvement over OI.

4.1.3 Advantages of Channel Synthesis

To emphasize the advantage of pursuing a multi-modal approach to surface ocean state estimation, we here test the extent to which GenDA can exploit observations of one variable to improve the predictions of others, i.e. its 'channel synthesis' capabilities. Firstly, the fact that GenDA captures significant variance and spatial structure in u_{ageo} and v_{ageo} despite assimilating no surface current observations demonstrates GenDA can exploit the physical relationships between satellite observables and ageostrophic currents learned from GLORYS during training (Figure 5 & Table 1).

GenDA ensemble mean predictions show increased R^2 across all variables in pixels where cloud-free L3 SST observations were assimilated compared to those occluded by clouds (Figure 10a). The improvement is (unsurprisingly) most clear for SST, as GenDA reconstructs almost all the variance in cloud-free pixels, demonstrating how closely the reconstruction converges to observations where provided. The next biggest improvement with cloud-free SST observations is for SSS, with R^2 (calculated on the residual from the low-resolution L4 SSS) almost doubling for cloud-free pixels. This makes it clear that frontal-scale SSS anomalies appear largely predictable given L3 SST and low-resolution L4 SSS. Frontal-scale SST and SSS anomalies are closely related likely because frontogenesis acts to amplify all surface tracer gradients simultaneously. There is also an improvement in R^2 for ageostrophic surface currents, likely due to the improved reconstruction of the strong frontal jets typically co-incident with strong density (and hence SST) gradients. The improvement in SSH is more limited in cloud-free pixels, possibly indicating that larger mesoscale SST signals, captured even in cloud-occluded regions by the low-resolution L4 SST input, drive most of the improvement seen in SSH mapping studies exploiting SSH-SST synergies (Archambault et al., 2023; Fablet et al., 2023, 2024; Martin et al., 2023, 2024b). Similarly, an increase in R^2 is observed across all variables in pixels where L3 SWOT SSH observations were assimilated (Figure 10b). SWOT SSH primarily appears to improve the reconstruction of ageostrophic currents and leads to relatively little improvement in SST or SSS. The improvement in ageostrophic currents is likely due to their relationship to SSH through cyclo-geostrophy (Penven et al., 2014; Cao et al., 2023). Taken together, Figure 10 shows the value in synergizing SSH and SST observations as they appear to provide ‘orthogonal’ information about the ocean state, with SSH containing information about the surface pressure and SST about the surface density.

4.1.4 Suitability of GenDA Ensemble for Uncertainty Quantification

Here we assess whether GenDA ensemble dispersion is a good metric of uncertainty. The spatial patterns of the ensemble dispersion, indicated by the ensemble standard deviation, for SSH and SST show a strong signature of the locations of L3 observations, with very low ensemble dispersion in SSH pixels observed by satellite altimeters and cloud-free SST pixels (Figure 11). In addition to the signature of the observing system, the SSH ensemble dispersion also appears elevated near strong SST fronts in the L3 observations, possibly indicating uncertainty in the SSH-SST phase shift for these fronts. However, ‘u-shaped’ rank histograms for all variables show that the GenDA ensemble is underdispersive (Figure 12). Concretely, the uncertainty estimate provided by the ensemble dispersion is an underestimation of the true predictive uncertainty: with the 24-member ensemble considered here, there is an up to 20% chance that the true value falls outside the range of ensemble members (adding the left and right bars in the rank histograms in Figure 12). Nonetheless, GenDA ensembles show no significant systematic biases even for the unobserved surface ageostrophic currents, as indicated by the symmetry of the rank histograms (Figure 12). Thus, despite slightly underestimating the spread, GenDA does provide a realistic-looking unbiased ensemble of eddy-scale predictions, representing an important advance compared to regression-type approaches.

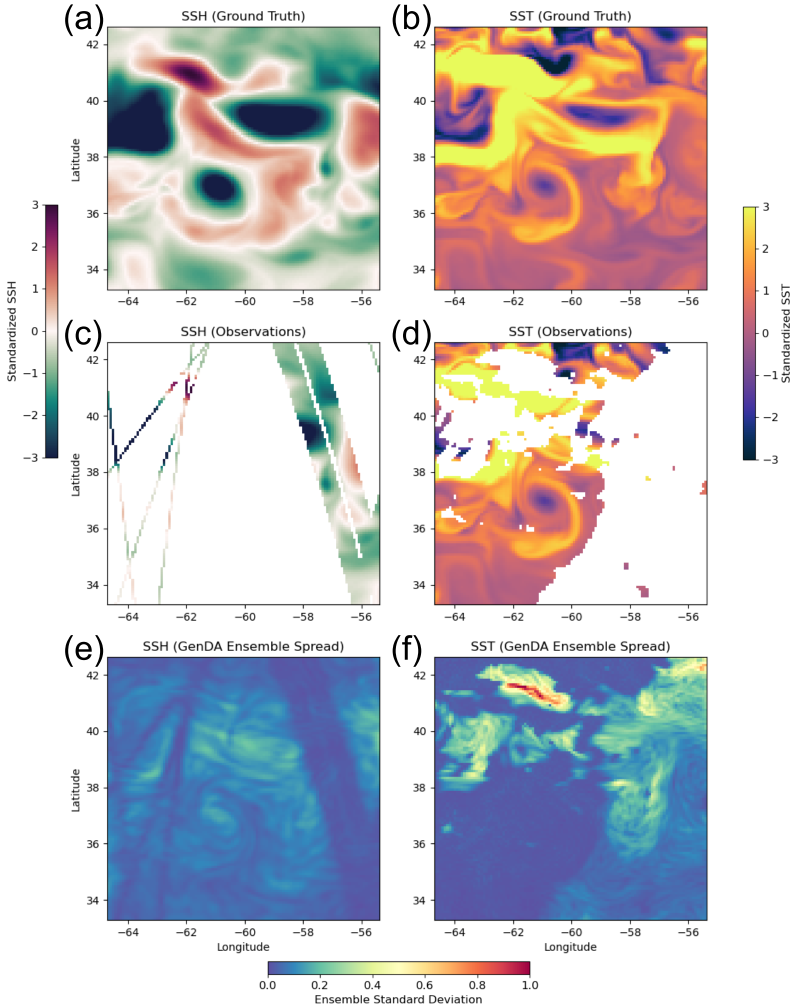

Figure 11. Ground truth target fields from GLORYS for (a) SSH and (b) SST. Simulated L3 observations assimilated for (c) SSH and (d) SST. GenDA ensemble standard deviation for (e) SSH and (f) SST.

4.2 Experiment 2 (OSE): Real-World Mapping Performance

4.2.1 SSH & SST Mapping Metrics

Assimilating real-world observations (Figure 13a-e), GenDA state estimations qualitatively look remarkably similar to those in the OSSE setting, encouraging confidence in its generalizability to real-world observations (Figure 13k-t). By contrast, the UNet Regression predictions (Figure 13f-j) appear significantly degraded, with unrealistic SST and SSS fields and ageostrophic surface current fields with significantly stronger variance than seen in GLORYS (Figure 5s,t). UNet Regression behaving poorly on real-world observations suggests that the network is overly sensitive to differences between real observations and the GCM pseudo-observations used in training, likely due to different noise properties and resolutions. GenDA ensemble member predictions (panels p-t) show enhanced variance at small scales, with realistic-looking frontal features in SST, SSS, and ageostrophic currents that are mostly absent in the low-resolution L4 gridded products assimilated (panels c-e).

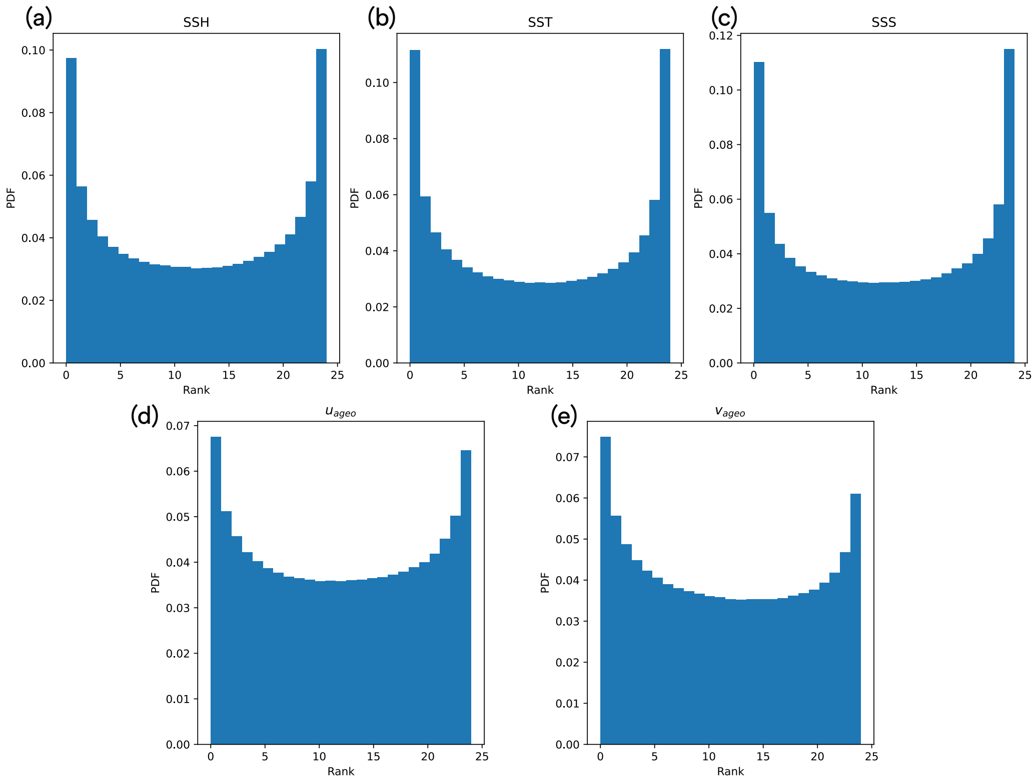

Figure 12. Rank histograms for GenDA OSSE predictions of (a) SSH, (b) SST, (c) SSS, (d) u_{ageo}, & (e) v_{ageo}. The x-axis represents the ordered ensemble members, while the y-axis is the probability density for the true value falling in each ensemble member bin. The first (last) bins represent truth values that lie below (above) the ensemble minimum (maximum). A well-calibrated ensemble has a flat-rank histogram.

The GenDA ensemble mean and ensemble members exhibit performance in SSH mapping metrics comparable to state-of-the-art methods (Figure 14a and Appendix A). This is perhaps not surprising since the ConvLSTM SSH maps were assimilated, but implies that adding four more variables to the state vector and requiring GLORYS-like dynamics does not lead to a significant drop in SSH mapping performance. By contrast, despite using the ConvLSTM SSH maps as input, UNet Regression shows severely degraded SSH mapping and fails to accurately resolve wavelengths as small as the DUACS OI method (Le Traon et al., 1998; Taburet et al., 2019). GLORYS 12 shows significantly worse SSH mapping errors, with its smallest resolved wavelength being more than double that of GenDA. This highlights the limitations of full 3D GCM data assimilation for resolving mesoscale surface eddies and the need for surface-only methods like GenDA. A similar picture emerges when assessing the SST mapping, with GenDA outperforming OI, UNet Regression, and GLORYS 12 (Figure 14b,c). The reduced R^2 in SST compared to in the OSSE setting are unsurprising since here our ground truth are L3 observations with significant sensor noise whereas in the OSSE we compared directly to the noise-free ground truth.

4.2.2 Spectral Evaluation & Eddy Dynamics

The spectra of SSH, SST, SSS, and geostrophic kinetic energy, after assimilation to real-world observations, show significant shifts from those of the GLORYS training

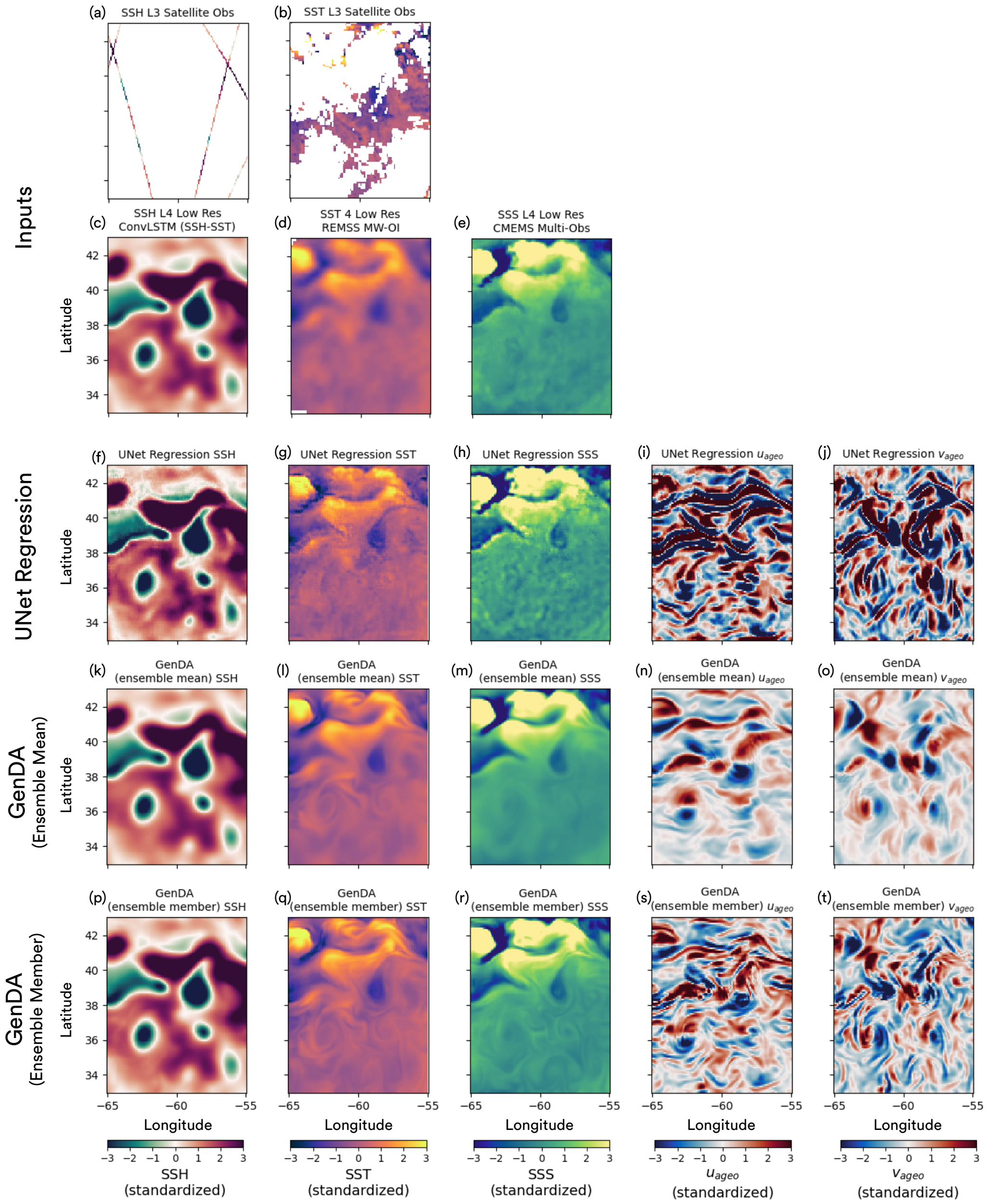

Figure 13. Example predictions for 2017-07-07 when assimilating real-world satellite observations in Experiment 2 (See S.I. Movie S2 for all dates). First row, input L3 observations assimilated: (a) SSH & (b) SST. Second row, input low-resolution L4 satellite products assimilated: (c), (d), & (e) SSH, SST, & SSS respectively. Third row, UNet Regression predictions for (f) SSH, (g) SST, (h) SSS, (i) u_{ageo}, and (j) v_{ageo}. Fourth row, (k)-(o) GenDA ensemble mean predictions. Fifth row, (p)-(t) GenDA ensemble member predictions. Note ERA 5 surface winds are also provided as input and predicted by GenDA but are not plotted since they match almost exactly.

data and the OSSE state estimates (Figure 15a-d). While in the OSE setting we don't have access to the ground truth spectra, the significant shift from GenDA (OSSE) to GenDA

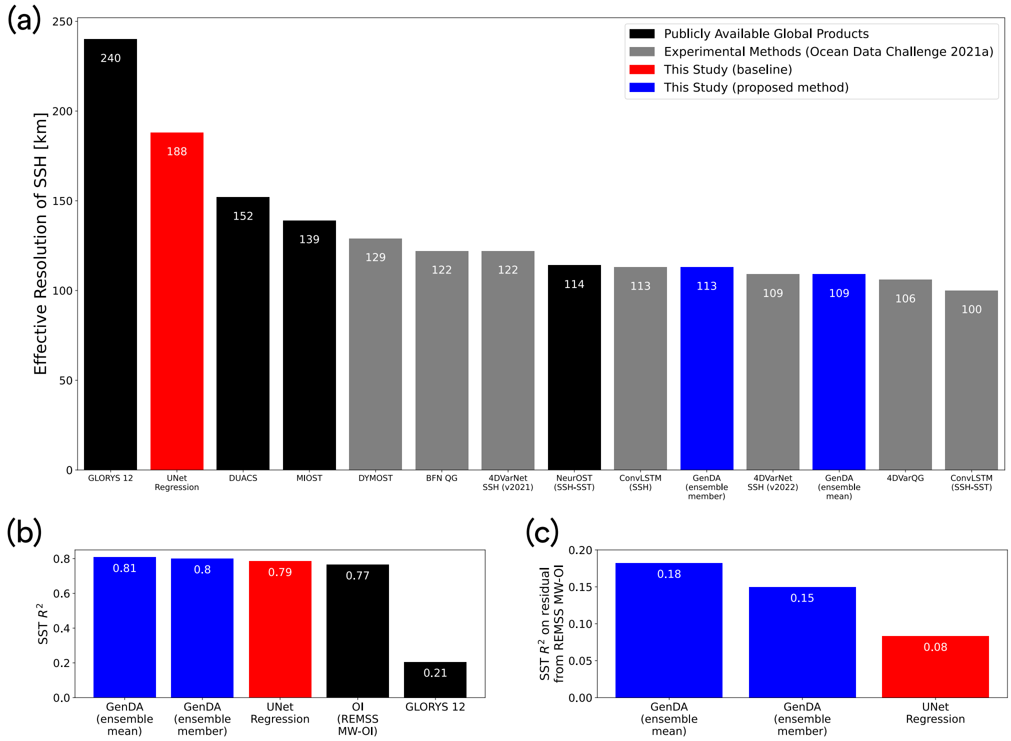

Figure 14. Accuracy of OSE state estimates against independent satellite observations. (a) Effective resolution, i.e. smallest resolved wavelength, of SSH for all methods in Ocean Data Challenge 2021a and those considered in this study. (Black) methods for which there are publicly available global products, (gray) experimental methods from other studies, (red) UNet Regression, and (blue) GenDA. (b) & (c) R^2 for SST compared to real-world L3 SST observations which were masked out by artificial clouds and not assimilated. (b) R^2 calculated directly on SST and (c) R^2 calculated on the residual from OI, meaning any positive value represents an improvement compared to OI.

(OSE), especially at larger scales, suggests the assimilation process allows the state estimates to adapt to real-world ocean conditions that are substantially different from the GLORYS training data. The GenDA reconstructions continue to exhibit power-law spectral slopes qualitatively similar to those in the OSSE setting and shallower than the L4 OI inputs, implying the diffusion prior learned from GLORYS ensures GenDA preserves realistic fine-scale features. By contrast, the UNet Regression spectra show substantially different shapes to those in the OSSE, further suggesting a lack of generalizability to real-world observations.

The GenDA spectra for ageostrophic kinetic energy remain qualitatively similar to those seen in the OSSE setting (Figure 15e), further increasing confidence that the GenDA reconstructions remain 'GLORYS-like' even after assimilating real-world observations. Intriguingly, despite no observations of ageostrophic surface currents being assimilated, the ageostrophic kinetic energy spectrum shows enhanced energy at large scales when assimilated to real-world satellite observations (Figure 15e). This suggests even the unobserved variables respond to changes in the spectral properties of the assimilated variables, and the change in large-scale ageostrophic kinetic energy could be a response to changes in the SSH spectrum (Figure 15a & d) through cyclogeostrophic balance (S.I.

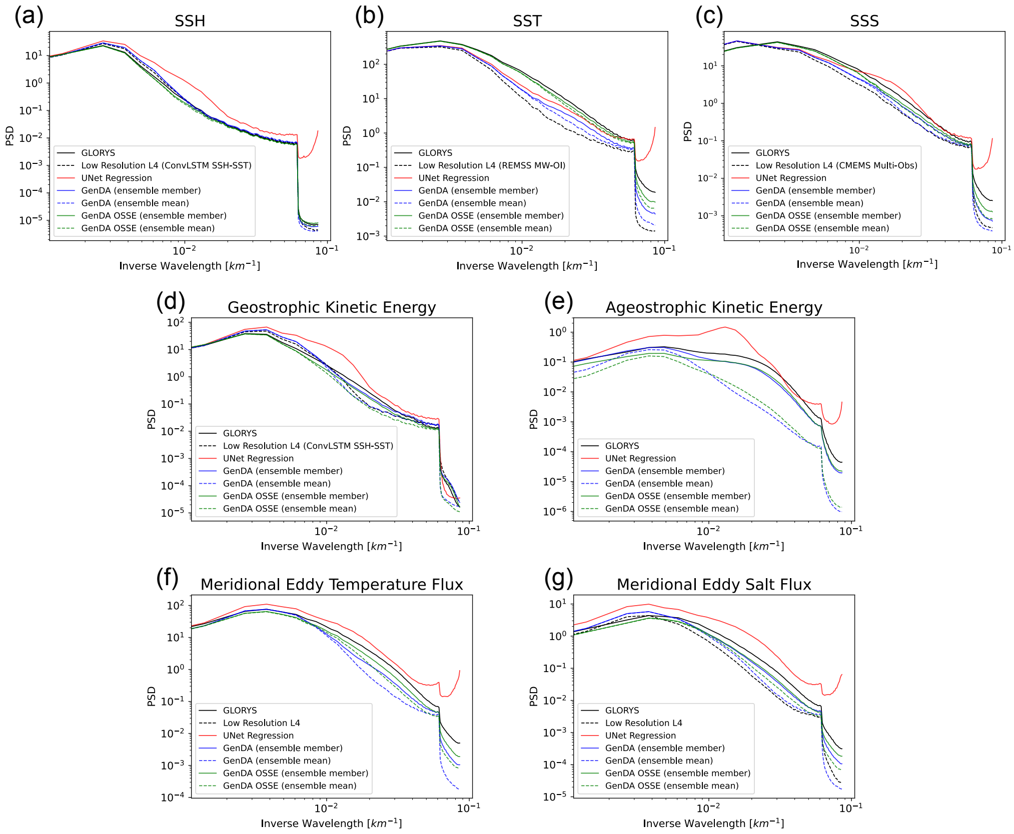

Figure 15. (a) SSH, (b) SST, (c) SSS, (d) geostrophic kinetic energy, (e) ageostrophic kinetic energy, (f) meridional eddy temperature flux, and (g) meridional eddy salt flux. (solid black) GLORYS reference from training (note this is no longer the ground truth when assimilating to real-world observations), (dashed black) low resolution L4 OI input assimilated, (solid red) UNet Regression, (solid blue) GenDA ensemble member, (dashed blue) GenDA ensemble mean, (solid green) GenDA ensemble member from the OSSE experiment on simulated observations, and (dashed green) GenDA ensemble mean from the OSSE experiment on simulated observations.

Text S7 & Figure S6) (Penven et al., 2014; Cao et al., 2023). The GenDA eddy flux spectra (Figure 15f,g) maintain their 'GLORYS-like' spectral slopes even when assimilated to real-world observations. Finally, the reconstructed geostrophic Okubo-Weiss fields from GenDA retain their qualitative realism from the OSSE setting (Figure 16), unlike the UNet Regression Okubo-Weiss which appears to deteriorate substantially. The significant differences in eddy placements in GLORYS 12 (Figure 16a) further highlight that full 3D GCM data assimilation and surface-only data assimilation yield substantially different results, with 3D state estimation coming at the expense of accurate placement of eddies at the surface.

5 Conclusions & Discussion

5.1 Conclusions

Score-based data assimilation (Rozet & Louppe, 2023a, 2023b), referred to here as GenDA, is a significant methodological departure from the regression approaches that

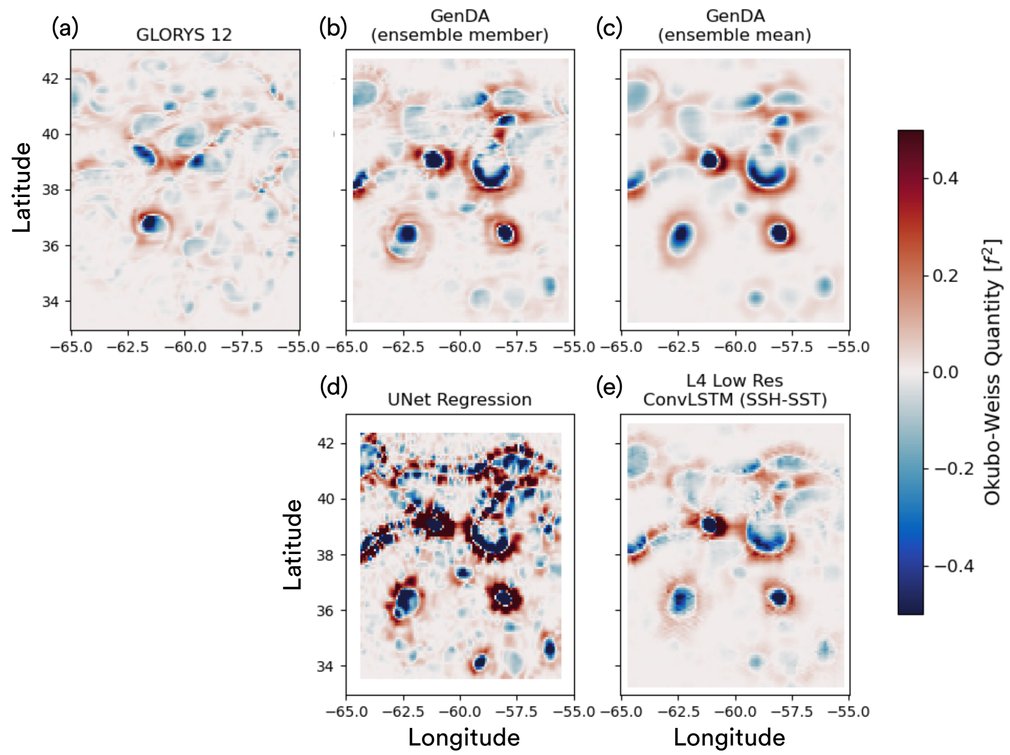

Figure 16. Geostrophic Okubo-Weiss quantity when assimilated to real-world observations for (a) GLORYS (no longer the ground truth in the OSE setting), (b) GenDA ensemble memner, (c) GenDA ensemble mean, (d) UNet Regression, and (e) OI. Negative values indicate vorticity dominates (as in eddy cores) whereas positive values show where strain dominates (as around eddy peripheries).

have to date been explored in deep learning satellite oceanography studies. By decoupling the neural network training from any specific observing system, GenDA provides a flexible and robust framework for guiding inference using a simulation-informed neural network with observations. GenDA improves the generalization from simulation training to real-world observations, retaining many dynamical characteristics of the simulation used during training. Enabling the use of multi-modal and multi-resolution observations resulted in significant benefits, with GenDA being now able to reconstruct ageostrophic currents and frontal-scale SSS from real-world satellite observations in an unsupervised manner (i.e. without any observations of currents or high-resolution salinity). By focusing solely on surface state estimation, GenDA reconstructions outperform state-of-the-art dynamical data assimilation systems, resolving SSH wavelengths twice as small as GLORYS 12 (Figure 14a). GenDA thus appears to provide a surface-only, neural alternative to 3D dynamical GCM data assimilation.

5.2 Discussion

While the results presented in this study represent a significant advance in eddy-resolving surface ocean state estimation, a number of limitations and areas for future method development should be noted. Our implementation of GenDA here works only on single temporal snapshots, meaning the GenDA reconstructions are not temporally coherent. GenDA predictions (both ensemble members and mean) for consecutive days show large jumps between time steps, especially for the high-resolution features that are only intermittently observed with L3 SSH and SST observations (S.I. Movies S1 & S2). Future work should therefore focus on extending the method to work on multiple time steps, potentially following the method proposed by Rozet and Louppe (2023a). Extending GenDA to assimilate multiple time steps may remove the need to assimilate low-resolution L4 satellite products in the observation operator by improving the geographic coverage of the L3 observations assimilated. Another limitation of the results presented here is the under-dispersiveness of the ensemble predictions. Future work could explore strategies for improving the realism of the reconstructed distribution, for example, through alternative reverse diffusion time-stepping schemes or data pre-processing steps. Since real-world OI products are not necessarily well-represented as a Gaussian coarse-graining operation, a promising direction for improving the spectral properties of GenDA state estimates would be to investigate the use of alternative filtering operations in the observation operator. Such efforts would be aided by studies of the spectral properties of low-resolution L4 OI products and how these can be approximated as filtering operations.

A fundamental limitation of the GenDA methodology is that the state estimate inherits its dynamical characteristics from the GCM simulation used during training. GCMs are imperfect representations of real-world ocean physics, and it is unclear to what extent GenDA would be able to 'un-learn' a simulation's biased physics during assimilation to observations. Since GenDA reconstructions are only as reliable as the GCM used during assimilation, one could consider it as a neural network analog to conventional data assimilation. Note that the high accuracy of the 2D surface ocean reconstruction is partially achieved by not formally satisfying GCM's 3D equations of motion, which themselves are known to be imperfect. For example, submesoscale-resolving SSH observations from SWOT are beginning to reveal that even frontier submesoscale-permitting ocean GCMs like LLC4320 (Su et al., 2018) can have significant statistical biases, including underestimation of the real-world ocean's submesoscale kinetic energy (Archer et al., 2025). The statistical discrepancies between simulation data and real-world observations, which are significant even in high-resolution models, emphasize the need to explore observation-only learning strategies for training high-resolution diffusion priors (Rozet et al., 2024).

There are many promising potential future research directions the GenDA method could enable. We here trained our diffusion prior on GLORYS 12 reanalysis data, but the grid resolution of the GCM used is too coarse to resolve submesoscale dynamics. In future, the GenDA diffusion prior could be trained on submesoscale-permitting free-running GCM's such as the $1/48°$ LLC4320 global simulation (Su et al., 2018) or the $1/60°$ NATL60 North Atlantic simulation (Ajayi et al., 2020). This would offer the tantalizing prospect of 'assimilating' frontier submesoscale GCMs to satellite observations, something that is beyond the current capabilities of conventional dynamical data assimilation. Training on submesoscale-permitting models could improve the realism of frontal dynamics by incorporating mixed layer instabilities into the training data, leading to potential improvements in our monitoring and understanding of ocean energy cascades (Sasaki et al., 2014; Klein et al., 2019; Taylor & Thompson, 2023). Submesoscale-permitting model training data, combined with a multi-timestep approach, could also enable GenDA in future to disentangle the effects of internal gravity waves and balanced submesoscale turbulence on SSH (H. Wang et al., 2022; Gao et al., 2024), a critical science requirement for the SWOT mission (Klein et al., 2019; Fu et al., 2024). The ability of GenDA to skillfully predict frontal scale SSS given cloud-free L3 SST and low-resolution L4 SSS from OI could in future be used to determine the extent to which SST fronts are salinity compensated (Rudnick & Ferrari, 1999), since SSS is not observed at frontal scales from satellites and theories of frontogenesis relate to density, not just SST (Hoskins, 1982). The flexibility to prescribe different observation operators for different observing systems make GenDA well-placed to exploit future proposed satellite missions directly measuring ageostrophic surface currents from space (Torres et al., 2023), to better exploit wide-swath altimetry (Fu et al., 2024), and to aid in future observing system design. Future studies could also consider how to assimilate other observing streams not typically assimilated in dynamical data assimilation, such as synthetic aperture radar (SAR), which contains signatures of both ocean turbulence and internal gravity waves (Ivanov & Ginzburg, 2002), or satellite ocean color observations, which show an abundance of submesoscale fronts and filaments (Lévy et al., 2018). These observations are not immediately amenable to assimilation through GenDA since these variables are not typically modeled in the ocean GCMs available for neural network training, and so new methods would be required to either model these variables within the GCM itself or to predict them as a post-processing step using GCM output. Finally, the ability of GenDA to reconstruct un-observed variables in an unsupervised manner suggests future studies could consider more ambitious dynamical quantities of interest in the state vector such as vertical velocities (Zhu et al., 2023; He & Mahadevan, 2024), air-sea fluxes, or interior ocean dynamics (George et al., 2021; Manucharyan et al., 2021).

Appendix A Complete Ocean Data Challenge 2021a SSH Evaluation Metrics (OSE)

Ocean Data Challenge 2021a SSH Mapping Metrics				
Method	RMSE Score, μ ($\uparrow$)	std of RMSE Score, σ ($\downarrow$)	Effective Resolution [km], λ_{eff} ($\downarrow$)	Notes
GenDA (ensemble mean)	0.90	0.06	109	Trained on GLORYS, reconstructs: SSH, SSS, SST, u, v
GenDA (ensemble member)	0.90	0.07	113	Trained on GLORYS, reconstructs: SSH, SSS, SST, u, v
UNet Regression	0.85	0.08	188	Trained on GLORYS, reconstructs: SSH, SSS, SST, u, v
GLORYS 12	0.73	0.13	240	1/12° GCM data assimilation (evaluation altimeter assimilated)
DUACS	0.88	0.07	152	OI as used in CMEMS product (SSH only)
MIOST	0.89	0.08	139	Dynamics-informed OI (SSH only)
DYMOST	0.89	0.06	129	Dynamics-informed OI (SSH only)
BFN QG	0.88	0.06	122	Data assimilation with QG model (SSH only)
4DVarNet (v2021)	0.89	0.06	122	Data assimilation-inspired neural network regression (SSH only)
4DVarNet (v2022)	0.89	0.09	109	Data assimilation-inspired neural network regression (SSH only)
4DVarQG	0.90	0.06	106	Data assimilation with QG model (SSH only)
ConvLSTM (SSH)	0.90	0.06	113	Neural network regression (SSH only)
ConvLSTM (SSH-SST)	0.90	0.06	100	Neural network regression (SSH & SST inputs, SSH output)
NeurOST (SSH-SST)	0.90	0.06	114	Neural network regression as used in PO.DAAC product (SSH & SST inputs, SSH output)

Table A1: Ocean Data Challenge 2021a SSH mapping metrics for the OSE. See Section 3.3.3 for metric details.

Open Research

We share the GenDA code through a public GitHub repository (`https://github.com/smartin98/GenDA`). All satellite and re-analysis datasets used in this study are publicly available and are cited in the text.

Acknowledgments

The research was funded by NASA Grant 80NSSC21K1187. P.K. acknowledges support from the SWOT Science Team, the QuickSCAT mission, and the S-MODE project. The authors gratefully acknowledge helpful discussions with Michele Buzzicotti, Quentin Febvre, Pierre Garcia, Peter Manshausen, and J. Xavier Prochaska. Our implementation of score-based data assimilation was based on code from Francois Rozet (`https://github.com/francois-rozet/sda`) and we trained our diffusion model using the NVIDIA Modulus framework (`https://github.com/NVIDIA/modulus`). Computational resources supporting this work were provided by the NASA High-End Computing (HEC) Program through the NASA Advanced Supercomputing (NAS) Division at Ames Research Center.

References

Agabin, A., Prochaska, J. X., Cornillon, P. C., & Buckingham, C. E. (2024). Mitigating masked pixels in a climate-critical ocean dataset. *Remote Sensing*, *16*(13).

Ajayi, A., Le Sommer, J., Chassignet, E., Molines, J.-M., Xu, X., Albert, A., & Cosme, E. (2020). Spatial and temporal variability of the north atlantic eddy field from two kilometric-resolution ocean models. *Journal of Geophysical Research: Oceans*, *125*(5), e2019JC015827.

Archambault, T., Filoche, A., Charantonis, A., & Béréziat, D. (2024). Pre-training and fine-tuning attention based encoder decoder improves sea surface height multi-variate inpainting. In *Visapp.*

Archambault, T., Filoche, A., Charantonis, A., Béréziat, D., & Thiria, S. (2024). Learning sea surface height interpolation from multi-variate simulated satellite observations. *Journal of Advances in Modeling Earth Systems*, *16*(6), e2023MS004047.

Archambault, T., Filoche, A., Charantonnis, A., & Béréziat, D. (2023). Multimodal unsupervised spatio-temporal interpolation of satellite ocean altimetry maps. In *VISAPP.*

Archer, M., Wang, J., Klein, P., Dibarboure, G., & Fu, L.-L. (2025). Global submesoscale ocean dynamics unveiled by wide-swath satellite altimetry. *Nature*, In press.

AVISO/DUACS. (2024). *SWOT level-3 KaRIn low rate SSH expert (v2.0) [Dataset].* CNES. Retrieved from `https://doi.org/10.24400/527896/A01-2023.018` (Accessed on 02-11-2024)

Ballarotta, M., Metref, S., Martin, S., Albert, A., Cosme, E., Beauchamp, M., & Le Guillou, F. (2021). *Ocean Data Challenges: 2021a SSH mapping OSE.* (`https://github.com/ocean-data-challenges/2021a_SSH_mapping_OSE`)

Ballarotta, M., Ubelmann, C., Pujol, M.-I., Taburet, G., Fournier, F., Legeais, J.-F., ... others (2019). On the resolutions of ocean altimetry maps. *Ocean Science*, *15*(4), 1091–1109.

Beauchamp, M., Febvre, Q., Georgenthum, H., & Fablet, R. (2022). 4DVarNet-SSH: end-to-end learning of variational interpolation schemes for nadir and wide-swath satellite altimetry. *Geoscientific Model Development Discussions*, *2022*, 1–37.

Bretherton, F. P., Davis, R. E., & Fandry, C. (1976). A technique for objective analysis and design of oceanographic experiments applied to mode-73. In *Deep sea research and oceanographic abstracts* (Vol. 23, pp. 559–582).

Buongiorno Nardelli, B., Cavaliere, D., Charles, E., & Ciani, D. (2022). Super-resolving ocean dynamics from space with computer vision algorithms. *Remote Sensing*, *14*(5), 1159.

Buzzicotti, M. (2023). Data reconstruction for complex flows using ai: Recent progress, obstacles, and perspectives. *Europhysics Letters*, *142*(2), 23001.

Cao, Y., Dong, C., Stegner, A., Bethel, B. J., Li, C., Dong, J., ... Yang, J. (2023). Global sea surface cyclogeostrophic currents derived from satellite altimetry data. *Journal of Geophysical Research: Oceans*, *128*(1), e2022JC019357.

Ciani, D., Fanelli, C., & Buongiorno Nardelli, B. (2024). Estimating ocean currents from the joint reconstruction of absolute dynamic topography and sea surface temperature through deep learning algorithms. *EGUsphere*, *2024*, 1–25.

Copernicus Climate Change Service (C3S. (2024). *Era5 hourly data on single levels from 1940 to present [Dataset].* Climate Data Store (CDS). Retrieved from `https://doi.org/10.24381/cds.adbb2d47` (Accessed on 09-24-2024)

Croitoru, F.-A., Hondru, V., Ionescu, R. T., & Shah, M. (2023). Diffusion models in vision: A survey. *IEEE Transactions on Pattern Analysis and Machine Intelligence*, *45*(9), 10850–10869.

Cushman-Roisin, B., & Beckers, J.-M. (2011). *Introduction to geophysical fluid dynamics: physical and numerical aspects.* Academic press.

E.U. Copernicus Marine Service Information (CMEMS). (2024a). *Global high resolution ODYSSEA sea surface temperature multi-sensor L3 [Dataset].* Marine Data Store (MDS). Retrieved from `https://doi.org/10.48670/mds-00329` (Accessed on 09-24-2024)

E.U. Copernicus Marine Service Information (CMEMS). (2024b). *Global ocean along track L3 sea surface heights reprocessed 1993 ongoing tailored for data assimilation [Dataset].* Marine Data Store (MDS). Retrieved from `https://doi.org/10.48670/moi-00146` (Accessed on 09-24-2024)

E.U. Copernicus Marine Service Information (CMEMS). (2024c). *Global ocean gridded normalized measurement noise of sea level anomalies [Dataset].* Marine Data Store (MDS). Retrieved from `https://doi.org/10.48670/moi-00144` (Accessed on 09-24-2024)

E.U. Copernicus Marine Service Information (CMEMS). (2024d). *Global ocean physics reanalysis [Dataset].* Marine Data Store (MDS). Retrieved from `https://doi.org/10.48670/moi-000216` (Accessed on 09-24-2024)

E.U. Copernicus Marine Service Information (CMEMS). (2024e). *Multi observation global ocean sea surface salinity and sea surface density [Dataset].* Marine Data Store (MDS). Retrieved from `https://doi.org/10.48670/moi-00051` (Accessed on 09-24-2024)

Fablet, R., Chapron, B., Drumetz, L., Mémin, E., Pannekoucke, O., & Rousseau, F. (2021). Learning variational data assimilation models and solvers. *Journal of Advances in Modeling Earth Systems*, *13*(10), e2021MS002572.

Fablet, R., Chapron, B., Le Sommer, J., & Sévellec, F. (2024). Inversion of sea surface currents from satellite-derived sst-ssh synergies with 4dvarnets. *Journal of Advances in Modeling Earth Systems*, *16*(6), e2023MS003609. doi: https://doi.org/10.1029/2023MS003609

Fablet, R., Febvre, Q., & Chapron, B. (2023). Multimodal 4dvarnets for the reconstruction of sea surface dynamics from sst-ssh synergies. *IEEE Transactions on Geoscience and Remote Sensing*, *61*, 1–14.

Fanelli, C., Ciani, D., Pisano, A., & Buongiorno Nardelli, B. (2024). Deep learning for super-resolution of mediterranean sea surface temperature fields. *EGUsphere*, *2024*, 1–18.

Febvre, Q., Le Sommer, J., Ubelmann, C., & Fablet, R. (2024). Training neural mapping schemes for satellite altimetry with simulation data. *Journal of Advances in Modeling Earth Systems*, *16*(7), e2023MS003959. doi: https://doi.org/10.1029/2023MS003959

Fu, L.-L., Pavelsky, T., Cretaux, J.-F., Morrow, R., Farrar, J. T., Vaze, P., … others (2024). The surface water and ocean topography mission: A breakthrough in radar remote sensing of the ocean and land surface water. *Geophysical Research Letters*, *51*(4), e2023GL107652.

Gao, Z., Chapron, B., Ma, C., Fablet, R., Febvre, Q., Zhao, W., & Chen, G. (2024). A deep learning approach to extract balanced motions from sea surface height snapshot. *Geophysical Research Letters*, *51*(7), e2023GL106623.

George, T. M., Manucharyan, G. E., & Thompson, A. F. (2021). Deep learning to infer eddy heat fluxes from sea surface height patterns of mesoscale turbulence. *Nature communications*, *12*(1), 800.

Ghosh, S., Sharma, A., Gupta, J., Subramanian, A., & Shekhar, S. (2024). Towards kriging-informed conditional diffusion for regional sea-level data downscaling: A summary of results. In *Proceedings of the 32nd acm international conference on advances in geographic information systems* (pp. 372–383).

Goh, E., Yepremyan, A. R., Wang, J., & Wilson, B. (2023). MAESSTRO: Masked autoencoders for sea surface temperature reconstruction under occlusion. *EGUsphere [pre-print]*, *2023*, 1–20.

Guo, Y., Bachman, S., Bryan, F., & Bishop, S. (2022). Increasing trends in oceanic surface poleward eddy heat flux observed over the past three decades. *Geophysical Research Letters*, *49*(16), e2022GL099362.
Han, Q., Jiang, X., Zhao, Y., Wang, X., Li, Z., & Zhang, R. (2024). Generative diffusion model-based downscaling of observed sea surface height over kuroshio extension since 2000. *arXiv preprint arXiv:2408.12632*.
He, J., & Mahadevan, A. (2024). Vertical velocity diagnosed from surface data with machine learning. *Geophysical Research Letters*, *51*(6), e2023GL104835.
Hersbach, H., Bell, B., Berrisford, P., Hirahara, S., Horányi, A., Muñoz-Sabater, J., ... others (2020). The era5 global reanalysis. *Quarterly Journal of the Royal Meteorological Society*, *146*(730), 1999–2049.
Hoskins, B. J. (1982). The mathematical theory of frontogenesis. *Annual Review of Fluid Mechanics*, *14*(1), 131–151.
Ivanov, A. Y., & Ginzburg, A. I. (2002). Oceanic eddies in synthetic aperture radar images. *Journal of Earth System Science*, *111*, 281–295.
Karras, T., Aittala, M., Aila, T., & Laine, S. (2022). Elucidating the design space of diffusion-based generative models. *Advances in neural information processing systems*, *35*, 26565–26577.
Klein, P., Lapeyre, G., Siegelman, L., Qiu, B., Fu, L.-L., Torres, H., ... Le Gentil, S. (2019). Ocean-scale interactions from space. *Earth and Space Science*, *6*(5), 795–817.
Kugusheva, A., Bull, H., Moschos, E., Ioannou, A., Le Vu, B., & Stegner, A. (2024). Ocean satellite data fusion for high-resolution surface current maps. *Remote Sensing*, *16*(7), 1182.
Lagerloef, G. S., Mitchum, G. T., Lukas, R. B., & Niiler, P. P. (1999). Tropical pacific near-surface currents estimated from altimeter, wind, and drifter data. *Journal of Geophysical Research: Oceans*, *104*(C10), 23313–23326.
Large, W., & Pond, S. (1981). Open ocean momentum flux measurements in moderate to strong winds. *Journal of physical oceanography*, *11*(3), 324–336.
Le Guillou, F., Chapron, B., & Rio, M.-H. (2024). Vardyn: Dynamical joint-reconstructions of sea surface height and temperature from multi-sensor satellite observations. *Authorea Preprints*.
Le Guillou, F., Gaultier, L., Ballarotta, M., Metref, S., Ubelmann, C., Cosme, E., & Rio, M.-H. (2023). Regional mapping of energetic short mesoscale ocean dynamics from altimetry: performances from real observations. *Ocean Science*, *19*(5), 1517–1527.
Le Guillou, F., Metref, S., Cosme, E., Ubelmann, C., Ballarotta, M., Le Sommer, J., & Verron, J. (2021). Mapping altimetry in the forthcoming SWOT era by back-and-forth nudging a one-layer quasigeostrophic model. *Journal of Atmospheric and Oceanic Technology*, *38*(4), 697–710.
Lellouche, J.-M., Greiner, E., Bourdallé-Badie, R., Garric, G., Melet, A., Drévillon, M., ... Le Traon, P.-Y. (2021). The copernicus global 1/12 oceanic and sea ice GLORYS12 reanalysis. *Frontiers in Earth Science*, *9*, 698876.
Le Traon, P., Nadal, F., & Ducet, N. (1998). An improved mapping method of multisatellite altimeter data. *Journal of Atmospheric and Oceanic Technology*, *15*(2), 522–534.
Lévy, M., Franks, P. J., & Smith, K. S. (2018). The role of submesoscale currents in structuring marine ecosystems. *Nature communications*, *9*(1), 4758.
Manshausen, P., Cohen, Y., Pathak, J., Pritchard, M., Garg, P., Mardani, M., ... Brenowitz, N. (2024). Generative data assimilation of sparse weather station observations at kilometer scales. *arXiv preprint arXiv:2406.16947*.
Manucharyan, G. E., Siegelman, L., & Klein, P. (2021). A deep learning approach to spatiotemporal sea surface height interpolation and estimation of deep currents in geostrophic ocean turbulence. *Journal of Advances in Modeling Earth Systems*, *13*(1), e2019MS001965.

Mardani, M., Brenowitz, N., Cohen, Y., Pathak, J., Chen, C.-Y., Liu, C.-C., … Pritchard, M. (2024). Residual diffusion modeling for km-scale atmospheric downscaling. *PREPRINT available at Research Square*. doi: https://doi.org/10.21203/rs.3.rs-3673869/v1

Martin, S. A., Manucharyan, G. E., & Klein, P. (2023). Synthesizing sea surface temperature and satellite altimetry observations using deep learning improves the accuracy and resolution of gridded sea surface height anomalies. *Journal of Advances in Modeling Earth Systems*, *15*(5), e2022MS003589.

Martin, S. A., Manucharyan, G. E., & Klein, P. (2024a). *Daily neurost l4 sea surface height and surface geostrophic currents. ver. 2024.0. [Dataset].* `https://doi.org/10.5067/NEURO-STV24`.

Martin, S. A., Manucharyan, G. E., & Klein, P. (2024b). Deep learning improves global satellite observations of ocean eddy dynamics. *Geophysical Research Letters*, *51*(17), e2024GL110059.

Metref, S., Ballarotta, M., Le Sommer, J., Cosme, E., Albert, A., Beauchamp, M., … Febvre, Q. (2023). *Ocean data challenges.* (`https://ocean-data-challenges.github.io/`)

Okubo, A. (1970). Horizontal dispersion of floatable particles in the vicinity of velocity singularities such as convergences. In *Deep sea research and oceanographic abstracts* (Vol. 17, pp. 445–454).

Penven, P., Halo, I., Pous, S., & Marié, L. (2014). Cyclogeostrophic balance in the Mozambique Channel. *Journal of Geophysical Research: Oceans*, *119*(2), 1054–1067.

Rai, S., Hecht, M., Maltrud, M., & Aluie, H. (2021). Scale of oceanic eddy killing by wind from global satellite observations. *Science Advances*, *7*(28), eabf4920.

Remote Sensing Systems. (2017). *Ghrsst level 4 mw-oi global foundation sea surface temperature analysis version 5.0 from REMSS [Dataset].* `https://doi.org/10.5067/GHMWO-4FR05`.

Ronneberger, O., Fischer, P., & Brox, T. (2015). U-net: Convolutional networks for biomedical image segmentation. In *Medical image computing and computer-assisted intervention–miccai 2015: 18th international conference, munich, germany, october 5-9, 2015, proceedings, part iii 18* (pp. 234–241).

Rozet, F., Andry, G., Lanusse, F., & Louppe, G. (2024). Learning diffusion priors from observations by expectation maximization. *arXiv preprint arXiv:2405.13712*.

Rozet, F., & Louppe, G. (2023a). Score-based data assimilation. *Advances in Neural Information Processing Systems*, *36*, 40521–40541.

Rozet, F., & Louppe, G. (2023b). Score-based data assimilation for a two-layer quasi-geostrophic model. *arXiv preprint arXiv:2310.01853*.

Rudnick, D. L., & Ferrari, R. (1999). Compensation of horizontal temperature and salinity gradients in the ocean mixed layer. *Science*, *283*(5401), 526–529.

Sasaki, H., Klein, P., Qiu, B., & Sasai, Y. (2014). Impact of oceanic-scale interactions on the seasonal modulation of ocean dynamics by the atmosphere. *Nature Communications*, *5*(1), 5636.

Seo, H., O'Neill, L. W., Bourassa, M. A., Czaja, A., Drushka, K., Edson, J. B., … others (2023). Ocean mesoscale and frontal-scale ocean–atmosphere interactions and influence on large-scale climate: A review. *Journal of climate*, *36*(7), 1981–2013.

Siegelman, L., Klein, P., Rivière, P., Thompson, A. F., Torres, H. S., Flexas, M., & Menemenlis, D. (2020). Enhanced upward heat transport at deep submesoscale ocean fronts. *Nature Geoscience*, *13*(1), 50–55.

Sinha, A., & Abernathey, R. (2021). Estimating ocean surface currents with machine learning. *Frontiers in Marine Science*, *8*, 672477.

Song, Y., & Ermon, S. (2019). Generative modeling by estimating gradients of the data distribution. *Advances in neural information processing systems*, *32*.

Su, Z., Wang, J., Klein, P., Thompson, A. F., & Menemenlis, D. (2018). Ocean submesoscales as a key component of the global heat budget. *Nature communications*, *9*(1), 775.

Taburet, G., Sanchez-Roman, A., Ballarotta, M., Pujol, M.-I., Legeais, J.-F., Fournier, F., ... Dibarboure, G. (2019). DUACS DT2018: 25 years of reprocessed sea level altimetry products. *Ocean Science*, *15*(5), 1207–1224.

Talagrand, O. (1999). Evaluation of probabilistic prediction systems. In *Workshop proceedings" workshop on predictability", 20-22 october 1997, ecmwf, reading, uk.*

Taylor, J. R., & Thompson, A. F. (2023). Submesoscale dynamics in the upper ocean. *Annual Review of Fluid Mechanics*, *55*, 103–127.

Torres, H., Wineteer, A., Klein, P., Lee, T., Wang, J., Rodriguez, E., ... Zhang, H. (2023). Anticipated capabilities of the odysea wind and current mission concept to estimate wind work at the air–sea interface. *Remote Sensing*, *15*(13), 3337.

Wang, H., Grisouard, N., Salehipour, H., Nuz, A., Poon, M., & Ponte, A. L. (2022). A deep learning approach to extract internal tides scattered by geostrophic turbulence. *Geophysical Research Letters*, *49*(11), e2022GL099400.

Wang, S., Li, X., Zhu, X., Li, J., & Guo, S. (2024). Spatial downscaling of sea surface temperature using diffusion model. *Remote Sensing*, *16*(20), 3843.

Weiss, J. (1991). The dynamics of enstrophy transfer in two-dimensional hydrodynamics. *Physica D: Nonlinear Phenomena*, *48*(2-3), 273–294.

Xiao, Q., Balwada, D., Jones, C. S., Herrero-González, M., Smith, K. S., & Abernathey, R. (2023). Reconstruction of surface kinematics from sea surface height using neural networks. *Journal of Advances in Modeling Earth Systems*, *15*(10), e2023MS003709.

Zhang, Z., Qiu, B., Klein, P., & Travis, S. (2019). The influence of geostrophic strain on oceanic ageostrophic motion and surface chlorophyll. *Nature Communications*, *10*(1), 2838.

Zhu, R., Li, Y., Chen, Z., Du, T., Zhang, Y., Li, Z., ... Wu, L. (2023). Deep learning improves reconstruction of ocean vertical velocity. *Geophysical Research Letters*, *50*(19), e2023GL104889.

Supporting Information for "Generative Data Assimilation for Surface Ocean State Estimation from Multi-Modal Satellite Observations"

Scott A. Martin[1], Georgy E. Manucharyan[1], and Patrice Klein[2,3,4]

[1]School of Oceanography, University of Washington, Seattle, WA, USA

[2]Environmental Science and Engineering, California Institute of Technology, Pasadena, CA, USA

[3]Jet Propulsion Laboratory, California Institute of Technology, Pasadena, CA, USA

[4]LMD-IPSL, ENS, PSL Université, Ecole Polytechnique, Sorbonne Université, CNRS, Paris, France

Contents of this file

1. Text S1 to S7
2. Tables S1 to S3
3. Figures S1 to S7

Additional Supporting Information (Files uploaded separately)

1. Captions for Movies S1 & S2

Text S1. Linear Ekman Regression Model for Wind-Driven Surface Currents

We remove both geostrophic currents and linear Ekman wind-driven currents from the total 15 m depth currents in GLORYS 12 as a pre-processing step before training GenDA (Equations 10 & 11).

The linear Ekman wind-driven current is given by

$$u_{Ek} = \frac{\sqrt{2}}{\rho_0 f d} e^{z/d} \left[\tau^x \cos\left(\frac{z}{d} - \frac{\pi}{4}\right) - \tau^y \sin\left(\frac{z}{d} - \frac{\pi}{4}\right) \right], \tag{S1}$$

and

$$v_{Ek} = \frac{\sqrt{2}}{\rho_0 f d} e^{z/d} \left[\tau^x \sin\left(\frac{z}{d} - \frac{\pi}{4}\right) + \tau^y \cos\left(\frac{z}{d} - \frac{\pi}{4}\right) \right], \tag{S2}$$

where d is the Ekman layer depth, z is depth, ρ_0 is a reference density, and τ^x and τ^y are the zonal and meridional wind stresses respectively (Equation 8.33 from Cushman-Roisin and Beckers (2011)). The Ekman layer depth, d, is a property of local oceanographic conditions which could vary geographically. The wind stresses can be estimated from ERA 5 surface winds using bulk aerodynamical formulae

$$\tau^x = \rho_a C_d u_{atmos} \sqrt{u_{atmos}^2 + v_{atmos}^2}, \tag{S3}$$

and

$$\tau^y = \rho_a C_d v_{atmos} \sqrt{u_{atmos}^2 + v_{atmos}^2}, \tag{S4}$$

where ρ_a is an atmospheric reference density which we take to be 1.2 kgm^{-3}, and C_d is a drag coefficient which we take to be 1.2×10^{-3} (Large & Pond, 1981).

In practice, we calculate wind stress from ERA 5 winds using Equations S3 & S4 and re-cast Equations S1 & S2 as a linear regression model

$$u_{Ek} = A(x, y)\tau^x + B(x, y)\tau^y, \tag{S5}$$

and

$$v_{Ek} = C(x, y)\tau^x + D(x, y)\tau^y, \tag{S6}$$

where A, B, C, and D are regression coefficients which we allow to vary geographically but assume to be fixed in time (Lagerloef et al., 1999). We find these coefficients by regressing Equations S5 & S6 at each coordinate onto GLORYS 12 ageostrophic surface currents over our full dataset duration (2010-2021).

Text S2. Why Include Surface Winds in the State Vector?

To improve the reconstruction of wind-driven currents not captured by our linear Ekman model (Text S1), we also reconstruct surface winds in the GenDA state estimate and assimilate ERA 5 winds in the observation operator. Here we show that assimilating ERA 5 winds improves the GenDA reconstruct skill for the unobserved ageostrophic surface currents (Table S1).

Text S3. Neural Network Architectures and Hyperparameters

Text S3.1. GenDA Diffusion Prior Architecture

The neural network architecture we use is a version of the UNet architecture (Ronneberger et al., 2015) with added self-attention used widely in diffusion models (Song & Ermon, 2019; Mardani et al., 2024). The full details of our architecture are illustrated in Figure S1. We use this architecture also for the UNet Regression baseline with minor modifications to the numbers of channels to accommadate observations in the input and to reduce overfitting observed during training.

Text S3.2. GenDA Generation Hyperparameters

Throughout this study, when generating state estimates using the diffusion prior we use the following hyperparameters. We discretize the the diffusion time axis into 256 steps from $t = 0$ to $t = T$, and follow the same time-stepping procedure as Rozet and Louppe (2023) and Manshausen et al. (2024). Although these prior studies used Langevin Monte Carlo correction steps, in this study we perform no correction steps as it was not found to improve performance in our experiments. We use the same noise schedule as Rozet and Louppe (2023),

$$\sigma(t) = \sqrt{1 - \mu(t)^2} \tag{S7}$$

$$\mu(t) = \cos(\omega t)^2 \tag{S8}$$

$$\omega = \arccos\left(\sqrt{10^{-3}}\right) \tag{S9}$$

where we set $T = 1$.

In Rozet and Louppe (2023) the heuristic variance for the posterior likelihood term in the main text (Equation 6) is

$$\mathcal{N}\left(y|\mathcal{A}(\hat{x}(t)), \Sigma_y(t)\right) = \mathcal{N}\left(y|\mathcal{A}(\hat{x}(t)), \Sigma_y + \frac{\sigma(t)^2}{\mu(t)^2}\Gamma\right), \tag{S10}$$

where Σ_y is the standard error of the observations, y, and Γ is a hyperparameter that controls the strength of the response to the observation likelihood term at higher noise levels. In this study we set $\Gamma = 0.1$, noting that this is slightly higher than the values used in Rozet and Louppe (2023) and Manshausen et al. (2024). We first tried smaller values for Γ but ran into numerical instabilities during generation so increased Γ until the generation stabilized.

Text S4. GLORYS Diffusion Prior Training Results

Here we present the training results for GenDA's score-based diffusion prior, D. During training, the diffusion model is trained to de-noise surface ocean state vectors from GLORYS 12 with Gaussian noise at varying amplitudes, $\sigma(t)$, added (Figure 2). The loss function, $\mathcal{L}_{EDM}$, minimized during training is MSE between the de-noised and noise-free state with a noise amplitude-varying weighting that has been found to improve training performance (Karras et al., 2022)

$$\mathcal{L}_{EDM} = \frac{\sigma(t)^2 + \sigma_{data}^2}{\left(\sigma(t) \cdot \sigma_{data}\right)^2} \left(D\left(x\left(t\right)\right) - x\left(0\right)\right)^2, \tag{S11}$$

where σ_{data} is a hyper-parameter which we set to 0.5, following Karras et al. (2022). We observe stable training with both training loss and validation loss decreasing throughout training before leveling off after $\sim 10^7$ training examples (Figure S2).

Sampling the diffusion prior unconditionally, i.e. with no assimilation of observations as described in Section 2.1.1, shows that our diffusion prior is able to largely capture the distribution of the GLORYS training data (Figure S3). For all variables, the diffusion prior appears able to produce realistic variability across all scales resolved in the GLORYS and ERA 5 training data. Intriguingly, unconditional generation appears to somewhat underestimate the variance consistently across all scales for all variables except SSH, which should be further investigated. We note though that assimilation observations mitigates this (see the results presented in the Main Text).

Text S5. Coarse-Graining Scales in GenDA Observation Operator

The GenDA observation operator requires the prescription of effective coarse-graining scales that reflect the resolutions of the low-resolution L4 SSH, SST, and SSS products assimilated (Section 2.1.3). Here we describe how we choose these scales for both experiments.

Text S5.1. OSSE: Scales Prescribed A Priori

In the OSSE, we simulate low-resolution L4 satellite products by coarse-graining the respective ground truth GLORYS field with a Gaussian kernel of width, σ_L, chosen to reflect what we expect to be the effective resolution of real-world satellite products. Since L4 satellite products also smooth in time, we smooth the ground truth in time with width, σ_T, when generating the simulated L4 products. Table S2 lists the coarse-graining scales chosen for each variable along with our rationale.

Since in the OSSE setting the effective coarse-graining scales of the L4 products are known, we set the coarse-graining scales in the GenDA observation operator to the same values used when generating the data (Table S2). Since GenDA operates only on snapshots, we neglect the temporal smoothing in the observation operator.

Text S5.2. OSE: Scales Tuned A Posteriori

In the real-world (OSE) setting, we assimilate real L4 products for which the effective coarse-graining scales are not known a priori. To select appropriate coarse-graining scales we therefore employ an a posteriori tuning strategy. We select the first day of each month from one of the cross-validation years (2019) to use as a dataset for tuning the coarse-graining scales. We then generate 120 random combinations of σ_{SSH}, σ_{SST}, and σ_{SSS} by uniformly sampling in the range [5, 40] km. We apply GenDA to the 12-day dataset for each coarse-graining scale combination and analyze the spectra of the resulting state estimates as well as compute errors against withheld SSH and SST observations.

SSH and SST reconstruction errors were found to co-vary only with σ_{SSH} and σ_{SST} respectively with no clear impact from σ_{SSS} on either and no co-variance between SSH and SST (Figure S4). We thus consider each variable to respond only to its respective coarse-graining scale in what follows. SSH and SST R^2 increase with decreasing σ_{SSH} and σ_{SST} respectively. This is likely due to the fact that decreasing the coarse-graining scale applied in the observation operator leads the GenDA state estimates to converge towards the low-resolution L4 products. The low-resolution L4 products are close to observations in terms of regression metrics, which are dominated by large-scale signals, but are overly-smooth compared to numerical simulations or L3 observations. When choosing σ_{SSH} and σ_{SST}, it is thus important not just to maximize R^2, but also to consider the impact on the physical realism of GenDA at small scales.

The spectral properties of SST on a near cloud-free day, 2019-09-01, illustrate the trade-offs between setting σ_{SST} too small or too large (Figure S5). When σ_{SST} is set too large, GenDA over-predicts variance at large scales relative to both OI and L3 observations to counteract the excessive smoothing applied in the observation operator (Figure S5a & b). Whereas setting σ_{SST} too small suppresses variance at small scales, pushing the GenDA state estimate towards OI and away from the L3 ground truth observations (Figure S5a & c). While choosing σ_{SST} is subjective, a rationale emerges looking at how the variance at large and small scales varies with σ_{SST} (Figure S5b & c respectively). We pick a value that is small enough for the large-scale variance to converge towards that predicted by OI, while being large enough to avoid the small-scale variance being suppressed too much. The small-scale variance in Figure S5c appears to roll off abruptly below $\sigma_{SST} \sim 15$ km which we take to be a symptom of σ_{SST} being too small below this threshold. To choose our OSE coarse-graining scales we thus look at how the large- and small-scale variance of GenDA SSH, SST, and SSS change with σ compared to the respective OI products (averaged over all 12 days in the tuning dataset) and pick values that appear to achieve the trade-off described above (Figure S6). This a posteriori tuning strategy leads us to values of 15 km for all variables (Table S3), which we note are in reasonable alignment with the values used in the OSSE (Table S2). Note, for SSH the small-scale variance didn't exhibit the clear roll-off at small σ that SST and SSS do (comparing Figure S6b to d & f), making our choice of σ_{SSH} more subjective. We instead inform our choice of σ_{SSH} by selecting the scale below which improvements in SSH R^2 plateau in Figure S4a.

Text S6. Weighted Re-Sampling Scheme for Comparing Errors For Cloudy vs Non-Cloudy SST and SWOT vs No SWOT SSH

In Figure 10, we compare state estimation errors between cases where L3 SST is cloud-occluded and cloud-free. Since the average cloud concentration has significant geographical structure, we need to ensure both the cloud-free and cloud-occluded datasets are drawn uniformly in space to ensure a fair comparison. We achieve this by drawing N samples from each dataset with replacement using a weighting function that compensates for the average cloud concentration to ensure the drawn samples are uniformly distributed in space.

We estimate the average cloud concentration, $C(x, y)$, through

$$C(x, y) = \overline{1 - f(x, y)}, \tag{S12}$$

where the overbar indicates averaging over all days in the test year 2017, and $f(x, y)$ is one for cloud-free pixels and zero for cloud-occluded pixels.

From the cloud concentration we then design weighting functions for both the cloud-occluded dataset,

$$W_{cloudy}(x, y) = \frac{1}{C(x, y)}, \tag{S13}$$

and for the cloud-free dataset,

$$W_{non-cloudy}(x, y) = \frac{1}{1 - C(x, y)}, \tag{S14}$$

and draw N samples with replacement using these weightings to scale the probability for each pixel to be drawn.

The same algorithm is used to compare errors when SWOT SSH is and isn't available, replacing cloud concentration with the fraction of days on which SWOT SSH was not available.

Text S7. OSE Ageostrophic Eddy Cyclo-Geostrophy Case Study

Here we highlight evidence of learned physics in the GenDA ageostrophic surface currents in the real-world setting, where we don't have a ground-truth reference field. To do this, we zoom in on the cyclonic eddy at 62°W 36°N in Figure 13 and compare the GenDA ageostrophic currents to those from an idealized theoretical calculation.

For an axially symmetric eddy in equilibrium, the next order correction to geostrophic balance, 'cyclo-geostrophy', has a closed form solution (Penven et al., 2014)

$$V = \frac{2V_g}{1 + \sqrt{1 + \frac{4V_g}{fR}}}, \tag{S15}$$

where V is the characteristic eddy velocity (taken here to be the maximum of the azimuthally averaged eddy velocity profile), V_g is the characteristic eddy velocity calculated from geostrophy, and R is the radius of the eddy. Note V and V_g are defined to be positive for a cyclone (anti-cyclone) in the Northern (Southern) Hemisphere and negative for the opposite rotation. Thus, in the Northern Hemisphere, cyclones are expected to be weaker than geostrophy predicts, and anti-cyclones are expected to be stronger.

For the cyclonic eddy in Figure S7a, the GenDA total surface current (we still don't add back in the Ekman current here to focus on eddy dynamics) is 10-15% weaker than the GenDA geostrophic current (Figure S7b-e). Applying cyclo-geostrophy to the GenDA geostrophic currents would lead to a 20-25% weakening of the current speeds (Figure S7f). The ageostrophic surface currents predicted by GenDA therefore appear to correct the eddy velocity in the direction expected from cyclo-geostrophy (i.e. the cyclone gets weaker), albeit with weaker magnitude than predicted from cyclo-geostrophy. The discrepancy between GenDA and cyclo-geostrophy could stem both from the idealizing assumptions of axial symmetry and equilibrium made in applying Equation S15, and from the fact that GenDA was observed to under-predict variance in ageostrophic currents in the OSSE setting (Table 1). We stress, GenDA is provided no observations of ageostrophic currents at inference and is here being assimilated to real-world satellite data, so it is predicting ageostrophic currents in a 'zero shot' manner. The simulation-informed diffusion prior therefore appears to have learned the physical relationships between unobserved ageostrophic currents and satellite observables (SSH/SST/SSS).

Movie S1. Movie of OSSE predictions for full testing year. Figure panels correspond to those in Figure 5.

Movie S2. Movie of OSE predictions for full testing year. Figure panels correspond to those in Figure 13.

References

Archambault, T., Filoche, A., Charantonis, A., Béréziat, D., & Thiria, S. (2024). Learning sea surface height interpolation from multi-variate simulated satellite observations. *Journal of Advances in Modeling Earth Systems*, *16*(6), e2023MS004047.

Cushman-Roisin, B., & Beckers, J.-M. (2011). *Introduction to geophysical fluid dynamics: physical and numerical aspects.* Academic press.

Karras, T., Aittala, M., Aila, T., & Laine, S. (2022). Elucidating the design space of diffusion-based generative models. *Advances in neural information processing systems*, *35*, 26565–26577.

Lagerloef, G. S., Mitchum, G. T., Lukas, R. B., & Niiler, P. P. (1999). Tropical pacific near-surface currents estimated from altimeter, wind, and drifter data. *Journal of Geophysical Research: Oceans*, *104*(C10), 23313–23326.

Large, W., & Pond, S. (1981). Open ocean momentum flux measurements in moderate to strong winds. *Journal of physical oceanography*, *11*(3), 324–336.

Manshausen, P., Cohen, Y., Pathak, J., Pritchard, M., Garg, P., Mardani, M., ... Brenowitz, N. (2024). Generative data assimilation of sparse weather station observations at kilometer scales. *arXiv preprint arXiv:2406.16947*.

Mardani, M., Brenowitz, N., Cohen, Y., Pathak, J., Chen, C.-Y., Liu, C.-C., ... Pritchard, M. (2024). Residual diffusion modeling for km-scale atmospheric downscaling. *PREPRINT available at Research Square*. doi: https://doi.org/10.21203/rs.3.rs-3673869/v1

Martin, S. A., Manucharyan, G. E., & Klein, P. (2024). Deep learning improves global satellite observations of ocean eddy dynamics. *Geophysical Research Letters*, *51*(17), e2024GL110059.

Penven, P., Halo, I., Pous, S., & Marié, L. (2014). Cyclogeostrophic balance in the

Mozambique Channel. *Journal of Geophysical Research: Oceans*, *119*(2), 1054–1067.

Ronneberger, O., Fischer, P., & Brox, T. (2015). U-net: Convolutional networks for biomedical image segmentation. In *Medical image computing and computer-assisted intervention–miccai 2015: 18th international conference, munich, germany, october 5-9, 2015, proceedings, part iii 18* (pp. 234–241).

Rozet, F., & Louppe, G. (2023). Score-based data assimilation. *Advances in Neural Information Processing Systems*, *36*, 40521–40541.

Song, Y., & Ermon, S. (2019). Generative modeling by estimating gradients of the data distribution. *Advances in neural information processing systems*, *32*.

Table S1: Effect of assimilating ERA 5 winds on GenDA (ensemble mean) reconstruction skill for ageostrophic currents.

ERA 5 Assimilated?	R^2 u_{ageo}	R^2 v_{ageo}
No	0.372	0.358
Yes	0.383	0.369

Table S2: Gaussian coarse-graining scales applied to SSH, SST, and SSS to generate simulated low-resolution L4 satellite products in the OSSE.

Variable	σ_L [km]	σ_T [days]	Rationale
SSH	25	1.75	Error analysis in Martin, Manucharyan, and Klein (2024).
SST	16	1.23	Same as chosen in Archambault, Filoche, Charantonis, Béréziat, and Thiria (2024).
SSS	16	1.23	Assumed to be same as SST.

Table S3: Gaussian coarse-graining scales applied to SSH, SST, and SSS in GenDA observation operator in OSE after a posteriori tuning.

Variable	σ_L [km]
SSH	15
SST	15
SSS	15

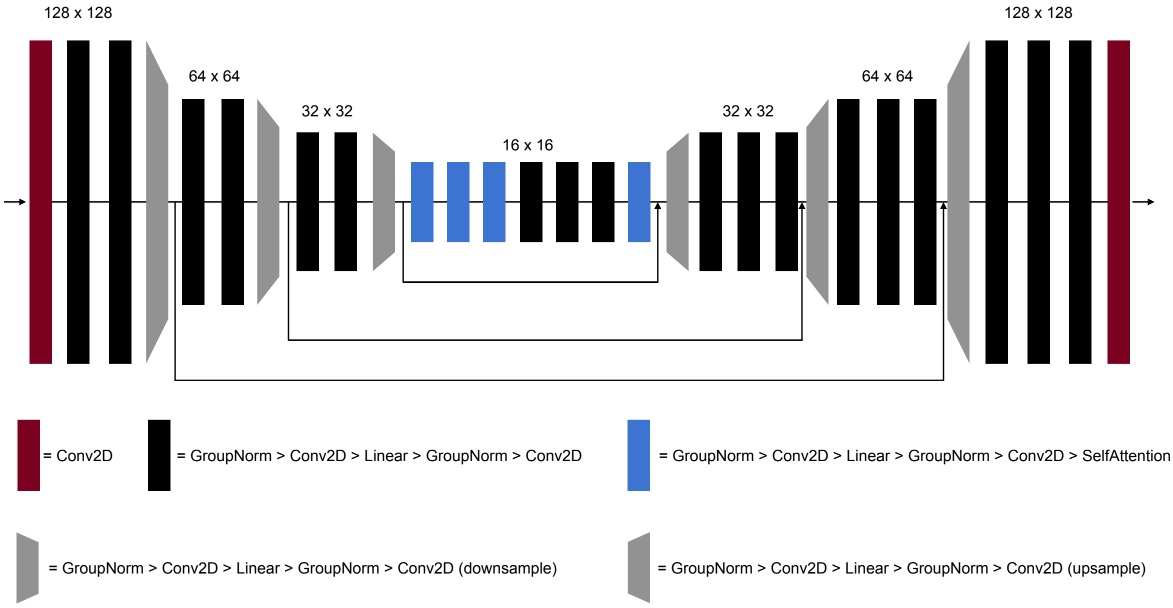

Figure S1: Schematic of the UNet neural network architecture used in both the GenDA diffusion prior and UNet Regression baseline.

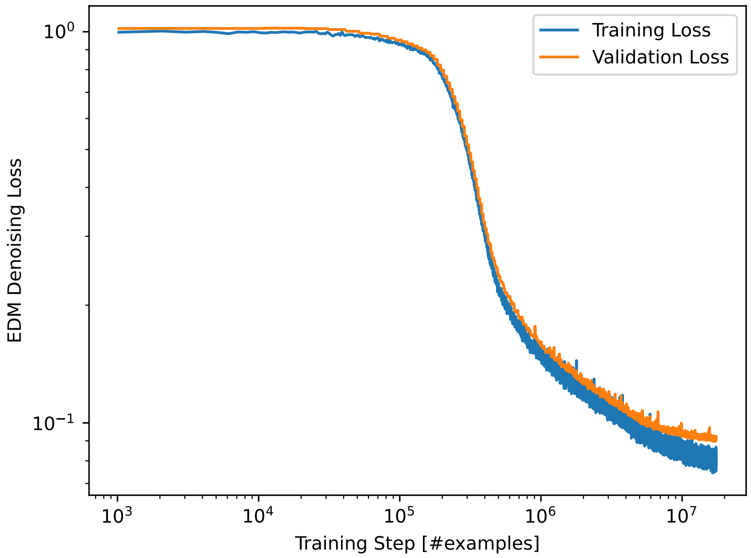

Figure S2: Learning curves for training the GenDA score-based diffusion prior to de-noise GLORYS 12 surface ocean states. The EDM de-noising loss function (Equation S11) is shown as a function of training step calculated both on the training (blue) and cross-validation (orange) datasets.

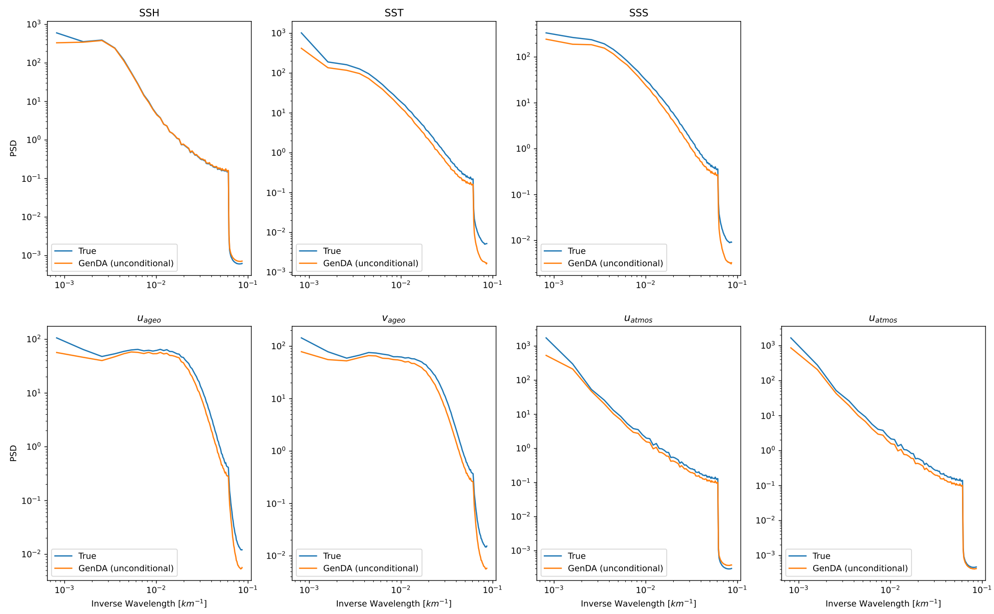

Figure S3: Spectra of each variable when generated unconditionally (with no assimilation of observations) by the GenDA score-based diffusion prior (orange) compared to the GLORYS ground truth (blue). (a) SSH, (b) SST, (c) SSS, (d) u_{ageo}, (e) v_{ageo}, (f) u_{atmos}, and (g) v_{atmos}.

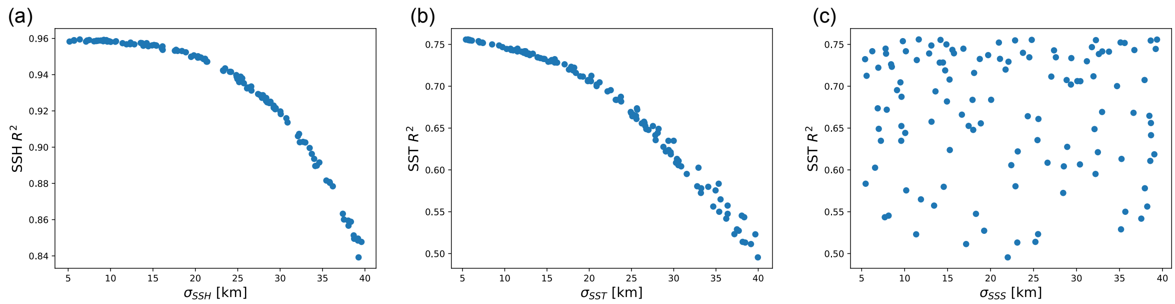

Figure S4: Effect of varying coarse-graining scales on GenDA OSE state estimate R^2 against independent L3 SSH and SST observations. (a) SSH R^2 with varying σ_{SSH}, (b) SST R^2 with varying σ_{SST}, and (c) SST R^2 with varying σ_{SSS}. No clear co-variance appears between SST R^2 and σ_{SSS}. We don't show them here, but co-variances between σ_{SSS} and SSH R^2, between σ_{SST} and SSH R^2, and between σ_{SSH} and SST R^2 are also not apparent with the plots looking like panel (c).

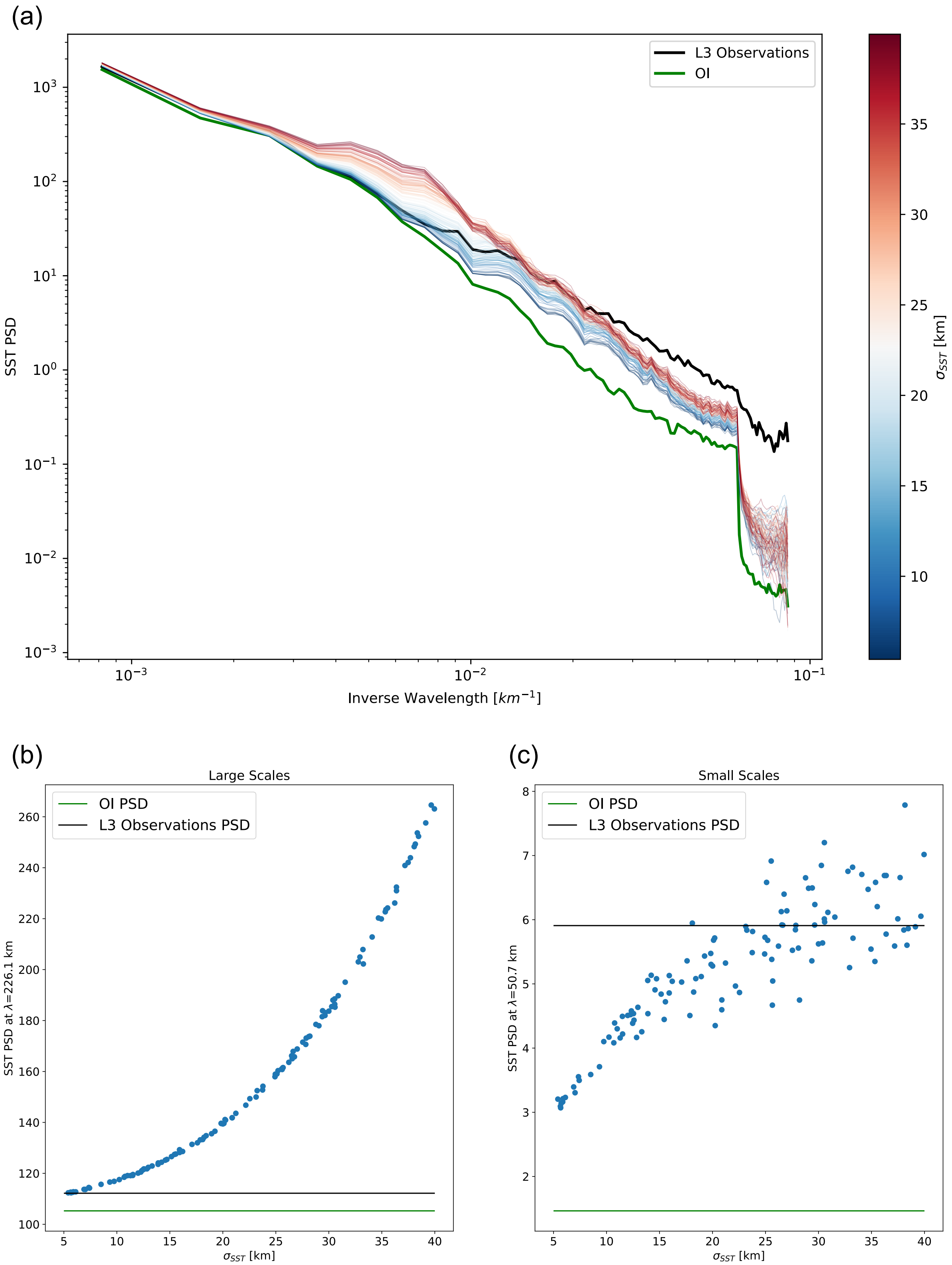

Figure S5: Spectral response of GenDA SST to varying σ_{SST} on a near cloud-free day of the tuning dataset, 2019-09-01. (a) SST spectra for GenDA with varying σ_{SST} (blue to red colormap), for L3 observations with the few cloudy pixels filled with the domain mean (black), and for the low-resolution L4 OI satellite product (green). The GenDA SST spectrum values at (b) a large wavelength ($\lambda = 226.1$ km) and (c) a small wavelength ($\lambda = 50.7$ km) are scattered against σ_{SST} and compared to L3 observations (black) and the low-resolution L4 OI satellite product (green).

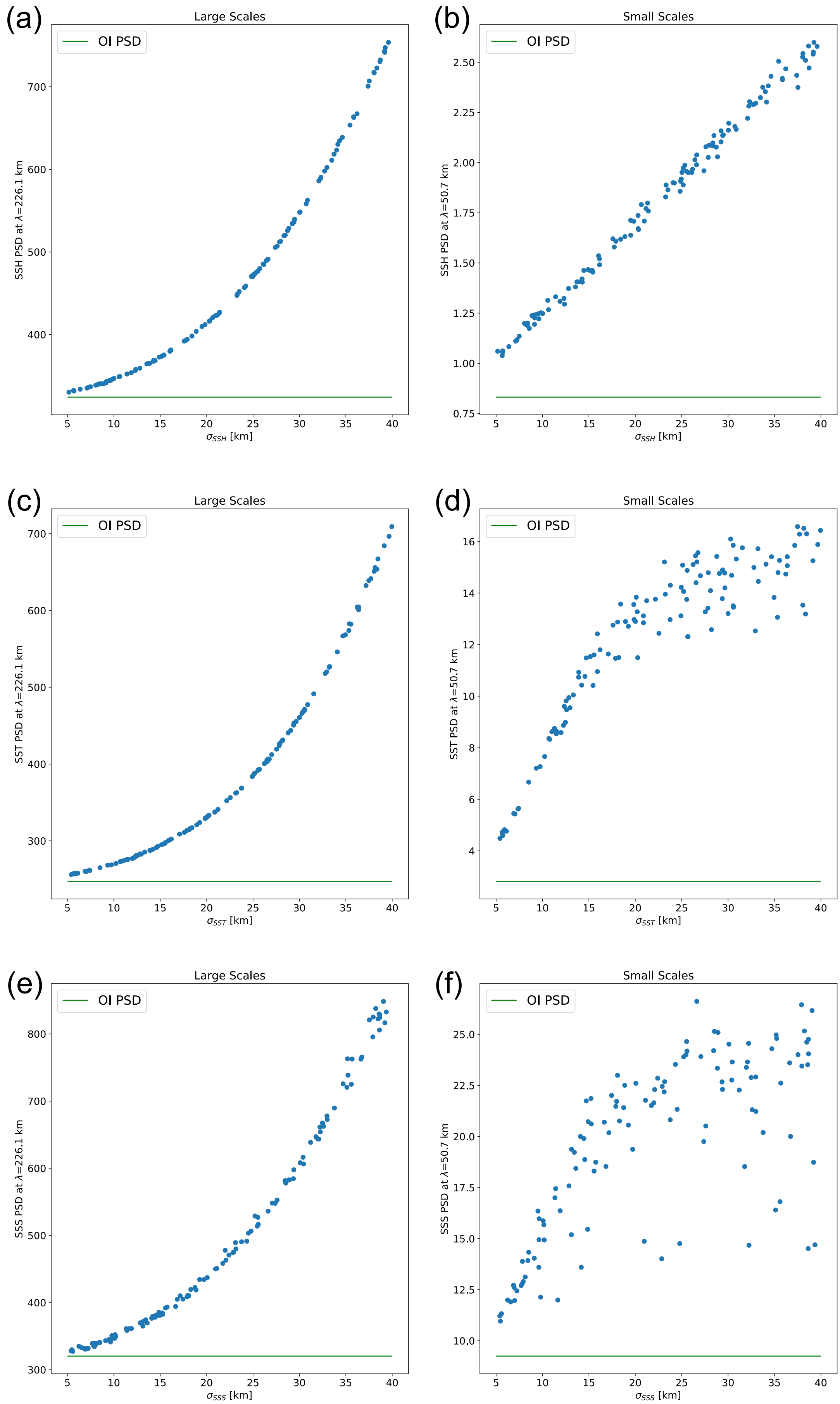

Figure S6: Spectral response of GenDA at large (λ = 226.1 km) and small (λ = 50.7 km) scales to varying coarse-graining scales averaged over all 12 days of the tuning dataset. (a) & (b) Large-scale and small-scale response of GenDA SSH to σ_{SSH} respectively. (c) & (d) Large-scale and small-scale response of GenDA SST to σ_{SST} respectively. (e) & (f) Large-scale and small-scale response of GenDA SSS to σ_{SSS} respectively. The low-resolution L4 OI satellite product is shown in green in all panels.

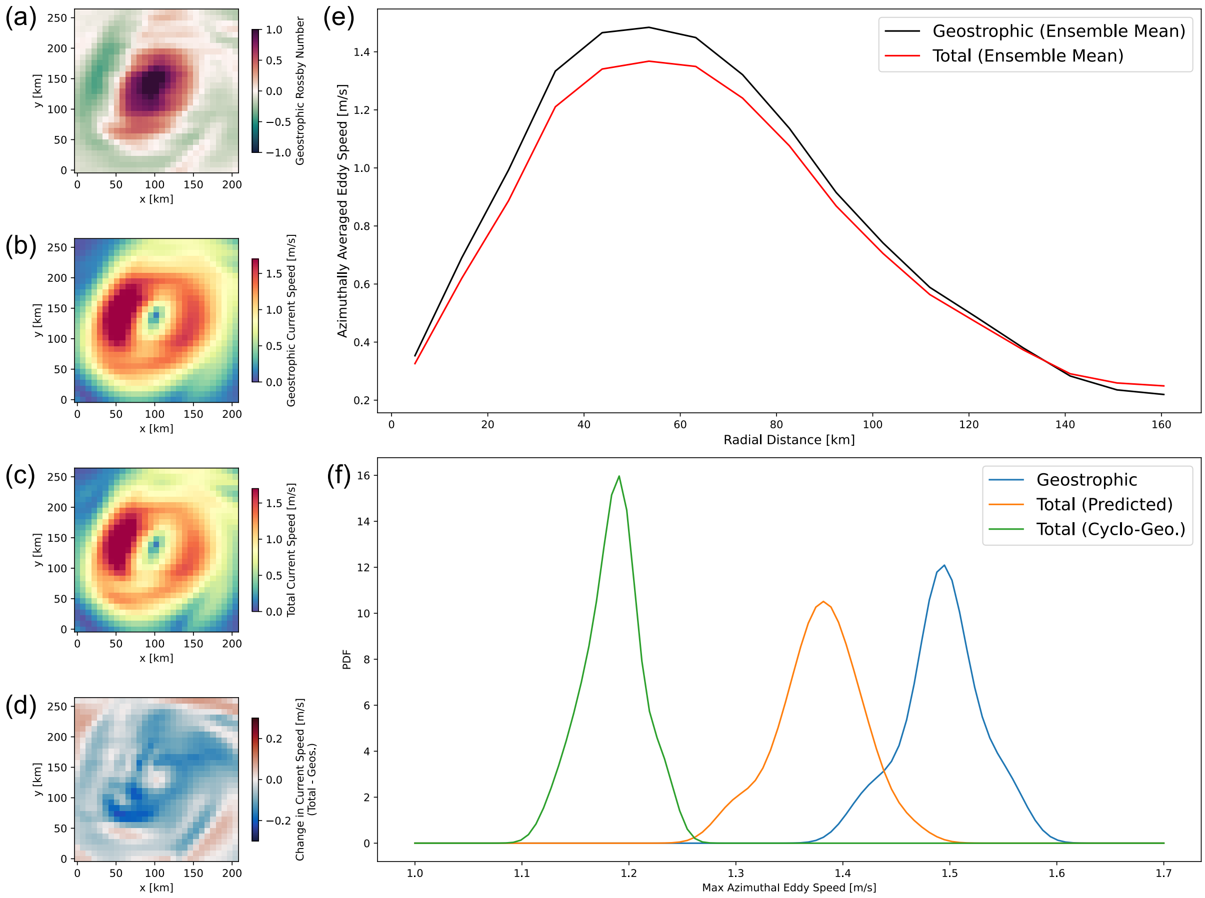

Figure S7: Comparing GenDA ageostrophic currents to cyclo-geostrophy for eddy reconstructed from real-world observations (cyclonic eddy at 62°W 36°N in Figure 13). Zoomed in view of the eddy in one of the GenDA ensemble members showing: (a) geostrophic vorticity, (b) geostrophic current speed, (c) total current speed (GenDA geostrophic plus GenDA ageostrophic), and (d) the change in speed between total and geostrophic currents. (e) Azimuthally averaged velocity profiles for geostrophic and total current speed, we show here the ensemble mean but each ensemble member looks qualitatively similar. (f) PDF over GenDA ensemble members of the eddy's characteristic speed for geostrophic currents, total currents, and solving cyclo-geostrophic balance using the geostrophic currents.